Revisiting Azimuthally Asymmetric Moist Instability in the Outer Core of Sheared Tropical Cyclones

Qingqing Li*

Pacific Typhoon Research Center, Key Laboratory of Meteorological Disaster of the Ministry of Education, Nanjing University of Information Science and Technology, Nanjing, and State Key Laboratory of Severe Weather, Chinese Academy of Meteorological Sciences, Beijing, China

Yufan Dai

Nanjing University of Information Science and Technology, Nanjing, China

January 4, 2019 (submitted)

May 15, 2019 (revised)

June 25, 2019 (revised)

September 20, 2019 (revised)

December 5, 2019 (revised)

Dateline

Submitted to ***Monthly Weather Review***

* Corresponding author address: Dr. Qingqing Li, School of Atmospheric Science, Nanjing University of Information Science and Technology, 219 Ningliu Road, Nanjing, Jiangsu 210044, China. Email: liqq@nuist.edu.cn

Early Online Release: This preliminary version has been accepted for publication in *Monthly Weather Review*, may be fully cited, and has been assigned DOI 10.1175/MWR-D-19-0004.1. The final typeset copyedited article will replace the EOR at the above DOI when it is published.

Abstract

This study revisits the characteristics and physical processes of the azimuthally asymmetric distribution of moist instability in the outer core of vertically sheared tropical cyclones (TCs) using a numerical model. The results indicate that a downshear-upshear contrast in outer-core conditional instability occurs in the weakly sheared TCs, while an enhanced downshear left-downshear right difference is found in strongly sheared storms. Specifically, lower (higher) conditional instability arises downshear left (right) in the strongly sheared TCs. Downward transports of low-entropy air by convective and mesoscale downdrafts in principal rainbands reduce the equivalent potential temperature (θ_e) in the downshear-left boundary layer, contributing to lower convective available potential energy. Positive horizontal advection of both potential temperature and water vapor by the asymmetric outflow leads to a midlevel maximum of θ_e in the same quadrant. Resultingly, a positive θ_e vertical gradient (thus potential stability) is present in the downshear-left outer core. In the downshear-right quadrant, a lack of convective downdrafts, together with surface fluxes, leads to higher θ_e in the boundary layer. A dry intrusion is found at the middle to upper levels in the downshear-right outer core, and significant negative horizontal advection of water vapor produces low θ_e near the midtroposphere. A negative vertical gradient of θ_e (thus potential instability) in the outer core arises below the downshear-right midtroposphere. The presence of azimuthally asymmetric moist instability is expected to play an important

Accepted for publication in *Monthly Weather Review*. DOI 10.1175/MWR-D-19-0004.1.

role in fostering and maintaining azimuthally asymmetric convective activity in the outer core of TCs.

Accepted for publication in *Monthly Weather Review*. DOI 10.1175/MWR-D-19-0004.1.

1. Introduction

It has been observationally and theoretically realized that environmental vertical wind shear (VWS) has prominent impacts on tropical cyclone (TC) structure and intensity change. Strong shear is documented to generally inhibit TC intensification (Frank and Ritchie 2001; Riemer et al. 2010; Tang and Emanuel 2010; Gu et al. 2015; Fu et al. 2019), and to force azimuthal asymmetries in convection (Jones 1995; Reasor et al. 2000; Frank and Ritchie 2001; Xu and Wang 2013; Reasor et al. 2013).

VWS generally produces an azimuthal wavenumber-1 asymmetry in eyewall convection with highest precipitation in the downshear-left quadrant (Jones 1995; Wang and Holland 1996; Reasor et al. 2000; Frank and Ritchie 2001; Corbosiero and Molinari 2002, 2003; Black et al. 2002; Xu and Wang 2013; Reasor et al. 2013; Barnes and Barnes 2014). Airborne Doppler radar observations (DeHart et al. 2014; Wadler et al. 2018) demonstrate that convective bursts in the vicinity of the eyewall typically initiate downshear right. As the convective bursts move cyclonically around the TC center, they develop vertically upward, reaching higher elevations in the downshear-left quadrant.

Marked asymmetries in convective activity are present in the outer core (roughly outside three times the radius of maximum wind; Wang 2009) of sheared TCs. Corbosiero and Molinari (2002), Stevenson et al. (2014), and Stevenson et al. (2016) examined flash locations in TCs, showing a strong preference for outer rainband flashes in the downshear-right quadrant. Many previous studies have indicated that convective

Accepted for publication in *Monthly Weather Review*. DOI 10.1175/MWR-D-19-0004.1.

cells within the part of the principal rainband in the downshear-right quadrant tend to collapse as they move into the downwind portion of the band where stratiform clouds become predominant (Hence and Houze 2008; Houze 2010; Didlake and Houze 2013). Li et al. (2017) documented that wavenumber-1 principal rainbands form downshear in sheared TCs, which is the result of the downshear-right convective reinvigoration of inner rainbands after they move outside the inner core. Riemer (2016) revisited the formation mechanism for the wavenumber-1 quasi-stationary band complex in the outer core of sheared TCs. He found that the overlap of regions of high-entropy air and a positive vorticity anomaly in lower layers on the right of the shear vector plays a fundamental role in initiating deep convection associated with the band complex.

Lift, instability, and moisture are the necessary conditions for the initiation of deep convection (Sherwood 2000; Schultz et al. 2000). The asymmetric distribution of moist instability occurs in the outer core of sheared TCs, hence possibly accompanying occurrences of asymmetric convection in the outer core. Observations indeed indicate that VWS enables azimuthally asymmetric distributions of moist instability within the TC circulation (Molinari and Vollaro 2008; Molinari and Vollaro 2010; Molinari et al. 2012). Molinari and Vollaro (2008) analyzed the combined data of dropsonde soundings and gridded analyses in Hurricane Bonnie (1998), indicative of much larger convective available potential energy (CAPE) values associated with downshear convective cells. They further extended the data to eight hurricanes (Molinari and Vollaro 2010), and a striking downshear-upshear difference in CAPE was found as well,

Accepted for publication in *Monthly Weather Review*. DOI 10.1175/MWR-D-19-0004.1.

with the average value of downshear CAPE about 60% greater than upshear CAPE for highly sheared storms. Moreover, Molinari et al. (2012) continued to address the CAPE calculation with and without condensate loading, entrainment, and latent heating of fusion based on more than 2000 dropsonde soundings, again confirming the circumstance of larger CAPE in the downshear semicircle within the 400-km radius from the storm center. They proposed that larger downshear CAPE results likely from higher surface moisture due to larger surface fluxes, cooler midlevel temperatures, and a more humid free-troposphere for entraining CAPE. Given the azimuthally asymmetric distribution of conditional instability mentioned above, convective cells are expected to preferentially form and develop in the quadrant where larger conditional instability exists, if air parcels are lifted.

Many studies have indicated an asymmetric, shear-induced entropy distribution within the TC boundary layer, and the azimuthally-varying vertical gradient of equivalent potential temperature (θ_e) possibly implies an azimuthal asymmetry in potential instability (Schultz and Schumacher 1999; Rosenow et al. 2018) within the TC circulation. For instance, Zhang and Rogers (2019) discussed the impact of the boundary layer structure on Hurricane Earl (2010)'s rapid intensification based on numerical simulations, illustrating lower (higher) θ_e predominantly downshear left (downshear right) both in the inner and outer cores (their Fig. 11). If significant potential instability arises in an individual quadrant, deep convection possibly develops there in the presence of layer lifting once the TC outer-core circulation interacts with a

Accepted for publication in *Monthly Weather Review*. DOI 10.1175/MWR-D-19-0004.1.

density current, front, or broad mountain range.

The studies mentioned above suggest a visible downshear-upshear contrast in moist instability in the outer core of sheared TCs, commonly with relatively higher instability in the downshear semicircle or sometimes particularly in the downshear-right quadrant. The release of azimuthally asymmetric instability is expected to play a salient role in generating and maintaining azimuthally asymmetric convective structures in the outer core. Moreover, the convective activity associated with azimuthally asymmetric moist instability in the outer core may have important effects on TC structure and intensity change. For instance, convection in spiral outer rainbands have been documented in previous studies to have marked impacts on TC intensity in various ways, usually suppressing TC intensification or weakening a TC (Barnes et al. 1983; Powell 1990a,b; Wang 2009; Li and Wang 2012a; Fu et al. 2019). Convective-scale downdrafts forced by convective cells in outer rainbands could bring low-entropy air downward into the boundary layer (Barnes et al. 1983; Powell 1990a,b; Hence and Houze 2008; Didlake and Houze 2009; Li and Wang 2012b). When such low-entropy air is further transported radially inward into the inner core of the TC, intensification would be suppressed, and the TC can weaken (Barnes et al. 1983; Powell 1990a,b; Li and Wang 2012a; Fu et al. 2019). Wang (2009) documented that diabatic heating produced by the convection in outer rainbands tends to lower the local near-surface pressure, thus reducing the horizontal pressure gradient across the radius of maximum wind and limiting TC intensity. Therefore, the azimuthally asymmetric distribution of moist

Accepted for publication in *Monthly Weather Review*. DOI 10.1175/MWR-D-19-0004.1.

instability in the outer core is likely to significantly modulate the convective activity of outer rainbands of sheared TCs, accordingly influencing the abovementioned detrimental role of outer rainbands in TC intensity.

Certain aspects regarding the azimuthally asymmetric moist instability still deserve further illumination as the asymmetric distribution of the instability likely dictates asymmetric convective activity in the outer core. For example, how is the degree of the asymmetry in outer-core conditional instability dependent on VWS magnitude? Does azimuthally asymmetric convective instability occur in the outer core of sheared TCs? In addition, fundamental physical processes giving rise to the occurrence of the azimuthally asymmetric moist instability in VWS still need further investigation. In this study, we thus revisit the traits of outer-core moist instability in sheared TCs, gleaning insights into the causes for the asymmetric distribution of the instability. Observations have shown that VWS associated with TCs generally has a wide variety of magnitudes when TCs are embedded within different environmental circulations (Rios-Berrios and Torn 2017). High-resolution numerical experiments will be conducted here to examine the characteristics of outer-core moist instability in TCs under environmental VWS with different magnitudes.

The present paper is organized as follows. In section 2, the model used and experimental design are outlined. The azimuthally asymmetric characteristics of conditional and potential instabilities, and physical processes modulating the instabilities, are present in sections 3 and 4, respectively. Section 5 summarizes the

Accepted for publication in *Monthly Weather Review*. DOI 10.1175/MWR-D-19-0004.1.

conclusions from the study.

2. Model and experimental design

The fully compressible, nonhydrostatic TC model, version 4 (TCM4), is used in this study, and a full description of TCM4 can be seen in Wang (2007). The physical parameterizations employed in TCM4 are summarized in Table 1. TCM4 has been used to successfully model a wide variety of TC structures, such as annular hurricanes (Wang 2008) and spiral rainbands (Wang 2009; Li and Wang 2012a,b; Li et al. 2017), and to investigate fundamental dynamics regarding TC structure and intensity change (Wang and Xu 2010; Fudeyasu and Wang 2011; Xu and Wang 2013; Li et al. 2014, 2015; Heng and Wang 2016).

In the present simulations, quadruply nested domains are employed with two-way interactive nesting, with domain sizes of 12960 km × 12960 km (D1), 2268 km × 2268 km (D2), 972 km × 972 km (D3), and 624 km × 624 km (D4). The grids have 32 vertical levels, and the horizontal grid intervals are 54, 18, 6, and 2 km, respectively. No cumulus parameterization is employed, even in the two outermost domains, as convection occurs mainly within the inner core of the modeled cyclone. The model is run on an *f*-plane at 18°N over the ocean with a fixed sea surface temperature of 29°C. An initial vortex has a maximum tangential wind velocity of 20 m s^{-1} at the 90-km radius near the surface, decreasing sinusoidally with pressure to zero at 100 hPa. The initial thermodynamic profile of the unperturbed model atmosphere is derived from the

Accepted for publication in *Monthly Weather Review*. DOI 10.1175/MWR-D-19-0004.1.

moist-tropical sounding of Dunion (2011).

After a 60-h spinup (T= 0 h assigned at this time), the minimum surface pressure of the simulated TC drops to approximately 965 hPa (Fig. 1), with a radius of maximum wind of 30 km and an evident warm core with a temperature anomaly exceeding 7 K near z = 8 km (not shown). At this time, easterly shears of 5, 15, and 25 m s^{-1} are introduced, respectively, with the zonal wind velocity increasing from 0 m s^{-1} at about z = 1.5 km to 5, 15, and 25 m s^{-1} at about z = 13.5 km and remaining constant above (see the inset in Fig. 1), respectively. Subsequently, the simulations continue for 48 hours. The sensitivity simulations of 5-, 15-, and 25-m s^{-1} shears are labeled SH05, SH15, and SH25, respectively. The 25th and 75th percentiles of the global distribution (4.5 and 11.0 m s^{-1}, respectively) of VWS were defined in Rios-Berrios and Torn (2017) as the lower and upper bound of moderate shear. Figure 4 in Rios-Berrios and Torn (2017) shows that the 25th and 75th percentiles of the shear relevant to North Atlantic hurricanes are subtly larger than those for the global TCs, with values of 5 and 12 m s^{-1}, respectively. Given the North Atlantic moist-tropical sounding of Dunion (2011) used as the initial thermodynamic profile of the model atmosphere, SH05, SH15, and SH25 imply the scenario of a TC in weak, strong, and extreme environmental vertical shears, respectively, especially for North Atlantic hurricanes. The experiment settings are identical to those in Li and Fang (2018).

Figure 1 shows the intensity evolution of TCs modeled in the three experiments. After a shear of 5 m s^{-1} is introduced in SH05, the storm still intensifies, with the

Accepted for publication in *Monthly Weather Review*. DOI 10.1175/MWR-D-19-0004.1.

minimum sea-level pressure dropping to about 922 hPa at 48 h. The intensity change substantiates that, to an extent, a TC under weak VWS can still intensify (Wang et al. 2015; Rios-Berrios and Torn 2017). For SH15, the simulated storm tends to weaken, exhibiting intensity oscillations. Such intensity oscillations are possibly associated with the quasi-periodic outer rainband activity (Li and Wang 2012a), or the vortex tilt and succeeding realignment (Reasor et al. 2004; Jones et al. 2009), which needs further investigation. As a very strong shear of 25 m s^{-1} is imposed in SH25, the TC rapidly weakens (Fig. 1), and then the vortex circulation becomes indistinct. Therefore, we will discuss only the first 12-h for SH25 thereafter.

3. Azimuthally asymmetric distribution of conditional instability in the outer core

a. CAPE and reflectivity

CAPE (Moncrieff and Miller 1976), roughly defined as the vertically integrated buoyancy of adiabatically lifted air, is generally used to evaluate the degree of conditional instability (Schultz et al. 2000). CAPE corresponds theoretically to convective activity (Weisman and Klemp 1982) and can be used to estimate the upper bound of the theoretical maximum updraft velocity. Therefore, it regularly acts as one of the environmental ingredients for moist convection (Emanuel 1994; Rasmussen and Blanchard 1998). As mentioned in the introduction, the asymmetric distribution of CAPE has been observed in sheared TCs. Such an asymmetry is revisited in this

Accepted for publication in *Monthly Weather Review*. DOI 10.1175/MWR-D-19-0004.1.

subsection. CAPE is defined as:

$$\text{CAPE} = \int_{LFC}^{EL} g \frac{T_v - T_{ve}}{\overline{T_{ve}}} dz, \qquad (1)$$

where T_v is the virtual temperature of the parcel; T_{ve} the virtual temperature of the environment; g the gravitational acceleration; z the vertical height; *LFC* the level of free convection; *EL* the equilibrium level; and the overbar represents the mean through the depth, *dz*. The values of CAPE in this study are calculated from vertical profiles and assume that an undiluted parcel is characterized by the mean humidity and temperature in the lowest 500 m.

Figure 2 depicts the horizontal distributions of modeled reflectivity at z = 3 km, superimposed by CAPE values. Consistent with prior findings, deep-layer VWS produces convective asymmetries in the inner core (approximately inside a 100-km radius here), with strongest convection in the downshear-left quadrant (Figs. 2a and 2b). Another prominent feature in SH15 is the preferred existence of principal rainbands (Willoughby et al. 1984; Willoughby 1988) outside the inner core. Such outer rainbands tend to arise downshear, and their formation is related closely to the convective reinvigoration of downshear inner rainbands (Li et al. 2017). Although a downshear outer rainband appears in SH05 at 24 h (Fig. 2a), visible outer rainbands also exist frequently in other quadrants (not shown). The preferentiality of wavenumber-1 principal rainbands is hence less significant in weak shear, although the convection in downshear outer rainbands seems to be more active (Fig. 2a) than that in other

Accepted for publication in *Monthly Weather Review*. DOI 10.1175/MWR-D-19-0004.1.

quadrants. As the shear increases up to 25 m s^{-1} (namely in experiment SH25), a reflectivity structure like a mesoscale convective system is positioned downshear left outside the inner core (Fig. 2c).

b. An overview of azimuthally asymmetric distribution of outer-core CAPE

CAPE within the TC circulation is characterized by azimuthal asymmetries in the experiments. In the experiment with weak shear (namely SH05), higher CAPE is located downshear at 24 h, and lower CAPE values occur upshear, with the lowest value upshear right outside a radius of 100 km (Fig. 2a). Such an asymmetry is also shown in the time-azimuth plot of CAPE radially averaged between 100 and 300 km (Fig. 3a). About 7 hours after the shear is imposed, a downshear-upshear contrast of CAPE occurs, with higher values in the downshear semicircle and lower values in the upshear semicircle (Fig. 3a). Molinari and Vollaro (2010) indicated that the mean values of CAPE in the downshear semicircle are comparable to those in the upshear semicircle for VWS < 10 m s^{-1}. The discordance between their results and the current study is because possibly the dropsonde soundings used in Molinari and Vollaro (2010) stemmed from eight hurricanes within diverse thermodynamic environments and were located mostly in the inner cores.

As the shear increases to 15 and 25 m s^{-1}, the wavenumber-1 asymmetric CAPE structure appears more pronounced, with higher (lower) values shifting to the right (left) of the shear vector (Figs. 2b and 2c), reminiscent of the results in Molinari et al. (2012).

Accepted for publication in *Monthly Weather Review*. DOI 10.1175/MWR-D-19-0004.1.

The value of CAPE in the downshear right quadrant is higher than that in other quadrants (Figs. 3b and 3c). Figures 3b and 3c further illustrate that CAPE in the downshear-left outer core is much lower than in other quadrants, particularly in the middle and downwind sectors of this quadrant. Also, higher convective inhibition (CIN) occurs upshear left (Figs. 3e and 3f). A similar asymmetric distribution of outer-core CAPE was observed in Hurricane Earl (2010) in Stevenson et al. (2014). Their Fig. 11 depicted the lowest CAPE values in the downshear-left outer core when Earl was experiencing VWS of approximately 8.5 m s^{-1}.

All in all, wavenumber-1 azimuthally asymmetric CAPE in the outer core of the sheared TCs is reproduced well in the numerical simulations, with higher CAPE located downshear for weak shear and highest values downshear right for strong shear. We will examine the causes of the asymmetric CAPE in SH15 and SH25 in the following subsections, mainly focusing on the downshear-right and downshear-left quadrants where CAPE values are vastly contrasting.

c. Higher CAPE in the downshear-right outer core

Molinari et al. (2012) pointed out that more considerable near-surface humidity, likely due to more significant surface fluxes in the downshear semicircle, plays a critical role in the existence of larger CAPE in that semicircle, although the near-surface temperatures were comparable downshear and upshear. The present simulations display that azimuthally asymmetric distributions of both near-surface temperatures and

Accepted for publication in *Monthly Weather Review*. DOI 10.1175/MWR-D-19-0004.1.

humidity are more striking in the strong and extreme shear environments (Figs. 4c, 4d, 4e, and 4f) than in the weak shear environment (Figs. 4a and 4b). In particular, much higher values of near-surface potential temperatures and humidity occur right-of-shear in SH15 and SH25 (Figs. 4c, 4d, 4e, and 4f), with maxima in the downshear-right quadrant. The difference, particularly in the downshear-upshear temperature contrast between Molinari et al. (2012) and the current study, is possibly owing to soundings in multiple TCs in Molinari et al. (2012), the storms most of which (> 85%) were in weak and moderate VWS and were likely embedded in different thermodynamic environments. As noted in Zhang et al. (2013) and Nguyen et al. (2017), although downshear-left downdrafts initially deposit drier air into the boundary layer, accumulated moistening via surface fluxes makes the boundary layer more humid right-of-shear as the air is advected cyclonically. There is thus much higher equivalent potential temperature (θ_e) air in the downshear-right outer core in SH15 and SH25 (Figs. 7b and 7c; discussed later), producing larger CAPE there (Figs. 3b and 3c).

The soundings in Molinari et al. (2012) show that there is the largest downshear-upshear temperature difference in the mid-troposphere, with colder air in the downshear semicircle, also contributing to the larger CAPE in the same semicircle. More significant midlevel temperature differences are also observed in the outer core in SH15 and SH25 (Figs. 5c and 5e), compared to SH05 (Fig. 5a). The mid-tropospheric air in the downshear-right quadrant is colder than that in the upshear-right quadrant (Figs. 5c and 5e). As a result, outer-core CAPE is the highest downshear right in SH15 and SH25.

Accepted for publication in *Monthly Weather Review*. DOI 10.1175/MWR-D-19-0004.1.

Figure 5d shows a weak intrusion of dry air at midlevels in the downshear-right outer core near a radius of 200 km in SH15. McCaul (1987) and Curtis (2004) hypothesized that dry air, which is ingested in the midtroposphere, would lead to an increase in evaporative cooling and steepen the lapse rate (thus a local increase in conditional instability). However, Fig. 6b suggests little latent cooling at midlevels in the downshear-right quadrant in SH15, and the strengthening of evaporative cooling associated with dry intrusions (McCaul 1987; Curtis 2004) seems not to be discerned. Indeed the occurrence of cooler potential temperatures at midlevels in the downshear-right quadrant (Figs. 5c) results from adiabatic cooling by convective-scale updrafts, which will be discussed later.

As mentioned in the introduction, Corbosiero and Molinari (2002), Stevenson et al. (2014), and Stevenson et al. (2016) revealed a strong downshear-right favorableness of lightning flashes in the outer rainbands. They stated that such a preference might be attributed to convection in the stationary band complex (Willoughby et al. 1984). Although the relationship between the downshear-right favorableness of flashes and the azimuthally asymmetric distribution of outer-core CAPE is not the subject of this study, we may make the following hypothesis. Li et al. (2017) demonstrated that environmental VWS preferably forces outer rainbands to form downshear. After the inner rainbands associated with vortex Rossby waves or triggered by flow deformation move outside the rapid filamentation zone, they convectively reinvigorate to form outer rainbands in the downshear semicircle because of not only reduced deformation but

Accepted for publication in *Monthly Weather Review*. DOI10.1175/MWR-D-19-0004.1.

also enhanced CAPE. With the development of the downshear outer rainbands, their upwind and middle sectors are located mainly in the downshear-right quadrant where CAPE is larger than in other quadrants, as revealed above. Convection with enhanced updrafts is likely fostered in the upwind and middle sectors of the rainbands (Hence and Houze 2008; Houze 2010), which facilitates the preference of flashes as observed in Corbosiero and Molinari (2002), Stevenson et al. (2014), and Stevenson et al. (2016).

d. Lower CAPE in the downshear-left outer core

Figures 3b and 3c indicate CAPE is much lower in the downshear-left quadrant than in other quadrants in SH15 and SH25. As noted above, the strong VWS yields a downshear preference of outer rainbands (namely principal rainbands; Li et al. 2017). The upwind, middle, and downwind portions of a well-developed outer rainband are accordingly characterized by nascent convective cells in the downshear-right quadrant, mature cells in the downshear-left quadrant, and stratiform clouds in the upshear-left quadrant, respectively (Hence and Houze 2008). Within a principal rainband, cooling due to rainwater evaporation can trigger convective-scale downdrafts close to the updraft core (Barnes et al. 1983; Powell 1990a,b; Didlake and Houze 2009; Li and Wang 2012b) and mesoscale subsidence in the downwind stratiform sector of the rainband (Riemer et al. 2010; Didlake and Houze 2013). One critical role of such sinking motion is to transport low-entropy air downward (Barnes et al. 1983; Powell 1990a,b; Li and Wang 2012a).

Accepted for publication in *Monthly Weather Review*. DOI 10.1175/MWR-D-19-0004.1.

Figure 6 depicts time-height cross sections of latent heating rate radially averaged between 100 and 300 km for the experiments, with the stippling denoting where sinking motion is located. In SH15 and SH25, relatively shallower, but larger, cooling is present in the downshear-left boundary layer (Figs. 6e and 6f), resulting mainly from the evaporation of rainwater in subsaturated air beneath convective clouds, and leading to low-level, convective-scale downdrafts (Didlake and Houze 2009; Li and Wang 2012b). In the upshear-left quadrant, deeper, but less, cooling dominates low to midlevels in SH15 (Fig. 6h), caused by rainwater evaporation underneath stratiform clouds (Fig. 2b; Riemer et al. 2010; Didlake and Houze 2013). Such low-level cooling is not apparent in SH25 (Fig. 6i) because stratiform precipitation is absent in the upshear-left quadrant in that extreme shear environment (Fig. 2c). As a result, cooling associated with the convective-scale downdrafts yields potential temperature minima between 100 and 200 km in the downshear-left quadrant (Figs. 4c and 4e) due to the evaporation of more precipitation. This evaporative cooling associated with the convective-scale downdrafts causes weaker conditional instability in the downshear-left quadrant. In the remaining quadrants, there is a lack of cooling relevant to intense sinking motion (Figs. 6b, 6c, 6k, and 6l). In contrast, no azimuthal preferentiality of evaporative cooling is observed in SH05 (Figs. 5a, 5d, 5g, and 5j) because weak VWS does not tend to initiate visible wavenumber-1 principal rainbands in this experiment.

In SH15 and SH25, the humidity between 100 and 200 km near the surface is much lower in the downshear-left quadrant than in other quadrants (Figs. 4d and 4f), resulting

Accepted for publication in *Monthly Weather Review*. DOI 10.1175/MWR-D-19-0004.1.

from the evaporationally induced downdrafts that transport drier air aloft downward (discussed later). Together with the potential temperature minima, much lower boundary-layer θ_e occurs downshear left (Figs. 7b and 7c). Although colder mid-tropospheric air occurs in the downshear-left quadrant (Figs. 5c and 5e), lower CAPE is still observed therein (Figs. 3b and 3c). This implies that the existence of much lower boundary-layer θ_e accounts mainly for the lower CAPE in the downshear-left quadrant.

Many previous studies have indicated that convective cells within the TC principal rainband tend to collapse as they move into the downwind portion of the band where broad stratiform clouds become predominant (Hence and Houze 2008; Houze 2010; Didlake and Houze 2013). Why do the cells weaken therein? Two reasons are hypothesized. One is the increased filamentation effect because the convection tracks more radially inward when cyclonically moving along the spiral rainband. The other is the visible decrease in conditional instability discussed above, which is just located in the middle and downwind sectors of the downshear-left quadrant. As the well-developed convective cells move more downwind, they thus tend to transition into stratiform clouds.

4. Azimuthally asymmetric distribution of potential instability in the outer core

a. An overview of the azimuthally asymmetric distribution of the θ_e vertical gradient

Figure 7 shows the time-quadrant distributions of θ_e in the three experiments for

Accepted for publication in *Monthly Weather Review*. DOI 10.1175/MWR-D-19-0004.1.

various heights, radially averaged between 100 and 300 km in different vertical layers. In SH05, there are noticeable downshear-upshear differences in θ_e vertically averaged between z = 0.1 and 0.96 km, particularly during 6–26 h and 37–48 h (Fig. 7a), with lower values in the upshear semicircle and higher values in the downshear semicircle. The averaged midlevel θ_e, whether it is downshear or upshear, is mostly lower than that in the boundary layer (Fig. 7d). Such a negative θ_e vertical gradient thus indicates potential instability in the outer core at low to midlevels. At upper levels, positive θ_e vertical gradients are present in all the quadrants (Figs. 7d and 7g).

As the magnitude of shear increases, the azimuthal asymmetry in outer-core θ_e becomes sharper. For example, higher θ_e averaged between z = 0.1 and 0.96 km in SH15 occurs right-of-shear, with peak values > 350 K downshear right (Fig. 7b). The minimum values of θ_e averaged between z = 0.1 and 0.96 km in SH15 are lower, compared to those in SH05, with the lowest θ_e values shifting to the downshear-left quadrant (Fig. 7b). The lower values of θ_e vertically averaged between z = 4.3 and 5.0 km exists on the right side of the VWS and higher θ_e is located left-of-shear, with maximum values > 343 K in the downshear-left quadrant (Fig. 7e). Similar asymmetric patterns are seen in SH25, with higher θ_e occurring in the downshear-left quadrant at mid- and upper-levels and occupying an azimuthally-compact area during 6 to 12 h of simulation (Figs. 7f and 7i). The patterns of θ_e vertically averaged between z =9.6 and 10.6 km in SH15 and SH25 resemble those in the midtroposphere, with the highest values (> 347 K) in the downshear-left quadrant (Figs. 7h and 7i).

Accepted for publication in *Monthly Weather Review*. DOI 10.1175/MWR-D-19-0004.1.

The above results thus show a notable negative vertical gradient of θ_e at low to midlevels in the downshear-right outer core in SH15 and SH25 (Figs. 7b, 7c, 7e, and 7f), suggestive of a potentially unstable environment. Above midlevels, θ_e increases with height in the same quadrant, indicative of the presence of potential stability. In the downshear-left outer core, there is a positive θ_e vertical gradient throughout the troposphere, demonstrating potential stability in that quadrant.

To further investigate the processes associated with the θ_e potential instability characteristics, θ_e budgets are conducted. The tendency equation for θ_e in TCM4 is

$$\frac{\partial\theta_e}{\partial t} = -\boldsymbol{V}_3 \cdot \nabla_3\theta - \frac{L}{C_p\pi}\boldsymbol{V}_3 \cdot \nabla_3 q_v + D_\theta + F_\theta + \frac{L}{C_p\pi}D_{q_v} + \frac{L}{C_p\pi}F_{q_v} + H_\theta, \qquad (2)$$

where $\boldsymbol{V}_3 \cdot \nabla_3 = u(\partial/\partial x) + v(\partial/\partial y) + w(\partial/\partial z)$, with u being the zonal wind, v the meridional wind, and w the vertical wind. In addition, θ, q_v, L, C_p, π, D_θ, F_θ, D_{q_v}, F_{q_v}, and H_θ denote the potential temperature, water vapor mixing ratio, latent heat, specific heat at constant pressure, Exner function, horizontal diffusion of potential temperature, vertical mixing of potential temperature including surface fluxes, horizontal diffusion of water vapor mixing ratio, vertical diffusion of water vapor mixing ratio, and dissipative heating, respectively. The detailed formulation of (2) can be found in Yang et al. (2007) and Li and Wang (2012a). The first two terms on the right side of (2) are the three-dimensional advective contributions of θ and q_v to the θ_e tendency, respectively. The remaining terms on the right are contributions by diabatic processes.

Accepted for publication in *Monthly Weather Review*. DOI 10.1175/MWR-D-19-0004.1.

Since the azimuthally asymmetric distribution of θ_e and potential instability is more notable in highly sheared TCs, particularly in the downshear semicircle, we further investigate in the following subsections the associated physical processes in these quadrants in SH15 and SH25 through the θ_e budgets.

b. The θ_e vertical gradient in the downshear-right outer core

Figure 8 displays the time-height cross sections of horizontal advection, vertical advection, diabatic processes, and total θ_e tendencies in SH15, which are radially averaged between 100 and 300 km in the downshear-right and downshear-left quadrants. Note that, although the total θ_e tendencies look somewhat noisy (Figs. 8d and 8h), some of the marked characteristics can still be discerned, which will be elaborated below.

Figures 8b and 8c show that the vertical advection and diabatic processes (mainly due to the surface fluxes, F_θ and F_{q_v}) contribute to the positive total θ_e tendency predominant below z = 3 km in the downshear-right quadrant, particularly during 0–30 h (Fig. 8d), although they are partly counteracted by the negative contribution of horizontal advection (Fig. 8a). Consequently, the θ_e value below z = 3 km increases in the downshear-right quadrant in SH15 during 0–30 h. For instance, the downshear-right θ_e value averaged within the boundary layer significantly increases during that time and is much higher than in other quadrants (Fig. 7b).

Negative horizontal advection between z = 4.5 and z = 11 km prevails particularly

Accepted for publication in *Monthly Weather Review*. DOI 10.1175/MWR-D-19-0004.1.

during 3–39 h (Fig. 8a), notwithstanding the positive vertical advection above z = 7 km (Fig. 8b). This negative horizontal advection contributes mainly to the negative θ_e tendency predominant between z = 4.5 and z = 10 km particularly before 24 h in SH15 (Fig. 8d). Figure 9 shows time-height cross sections of mean contributions by the horizontal and vertical advection of θ and q_v to the θ_e tendency in SH15. Weak horizontal advection of θ is present in upper layers (e.g., 9.6–10.6 km; Fig. 9a), resulting from the outer-core asymmetric wind vectors in the downshear-right quadrant approximately parallel with the isotherms (Fig. 10c). There exists a pronounced dry air slot between 150- and 250-km radii in the downshear-right quadrant in upper layers (Fig. 10d). Note that, comparatively, no dry tongue is found in upper layers in SH05 (Fig. 10b). Therefore, this upper-level dry tongue in SH15 results likely from the dry intrusion by the enhanced upper-layer TC-relative outflow. A weaker dry intrusion in the midtropospheric outer core is also found downshear right (Fig. 5d), as noted in subsection 3b. Therefore, the horizontal advection of q_v averaged in the downshear-right quadrant in SH15 becomes predominantly negative between z = 4.5 and z = 11 km during most of the 48-h simulation time (Fig. 9b). The horizontal advective contribution to the θ_e tendency between z = 4.5 and z = 11 km is thus mostly negative in that quadrant particularly during 3–39 h (Fig. 8a), responsible for the negative total θ_e tendency between z = 4.5 and z = 10 km particularly before 12 h (Fig. 8d), as mentioned above. Consequently, the outer-core θ_e values in both middle and upper layers in SH15 subtly decrease in the downshear-right quadrant before 12 h (Fig. 7h).

Accepted for publication in *Monthly Weather Review*. DOI 10.1175/MWR-D-19-0004.1.

The above analysis indicates that the negative θ_e vertical gradient (hence potential instability) below the midtroposphere in the downshear-right outer core (Figs. 7b and 7e) results from higher θ_e values relevant to the positive θ_e tendency below z = 3 km and lower θ_e values associated with the negative θ_e tendency between z = 4.5 and z = 11 km in that quadrant (Fig. 8d). Although the outer-core θ_e value at upper levels in the downshear-right quadrant decreases particularly before 24 h (Fig. 7h) due to the negative total θ_e tendency, it is still higher than that at midlevels in the same quadrant (Fig. 7e). There thus exists potential stability above the midtroposphere in the downshear-right quadrant in SH15.

As the VWS is increased up to 25 m s^{-1} (namely in SH25), the general characteristics of the θ_e budget in the outer core on the right of VWS resemble those in SH15. For instance, positive θ_e tendencies prevail beneath the downshear-right midtroposphere (Fig. 11d), yielding a marked increase in θ_e in the downshear-right boundary layer (Fig. 7c). In contrast, negative θ_e tendencies abound above the midlevels (Fig. 11d), making the upper-level θ_e value decrease in the downshear-right quadrant in SH25 (Fig. 7i). Positive horizontal advection of θ is observed mostly in the downshear-right troposphere, and a maximum that is larger than in the downshear-right quadrant in SH15 (Fig. 9a) occurs around z = 4–5 km (Fig. 12a). Negative horizontal advection of q_v primarily dominates in the same quadrant, also with a midlevel minimum (Fig. 12b) that is much smaller than in SH15 (Fig. 9b). As a result, a downshear-right positive (negative) horizontal advection contribution occurs below

Accepted for publication in *Monthly Weather Review*. DOI 10.1175/MWR-D-19-0004.1.

(above) approximately z = 4 km, mainly after 4 h in SH25 (Fig. 11a). In addition, the positive vertical advective contribution of q_v surpasses the negative vertical advective contribution of θ (Figs. 12c and 12d), leading to the predominant positive vertical advection below z = 3 km (Fig. 11b). Along with the positive contribution of surface fluxes (Fig. 11c), positive θ_e tendencies thus occur below the midlevels in the downshear-right quadrant (Fig. 11d), contributive to the increase in θ_e and the higher boundary-layer θ_e value in that quadrant (Fig. 7c). The positive θ_e tendencies below the downshear-right midtroposphere in SH25 (Fig. 11d) are larger than those in SH15 (Fig. 8d), making the boundary-layer θ_e value in the downshear-right quadrant increase more rapidly in SH25 than in SH15 during the first 12-h simulation (Figs. 7b and 7c). The negative horizontal advective contribution above z = 4 km after 4 h mainly produces negative θ_e tendencies above the same altitude (Fig. 11d), resulting in a significant decrease in θ_e and making the θ_e value near z = 5 km lower in the downshear-right quadrant than in other quadrants (Fig. 7f). The downshear-right negative θ_e tendencies near z = 5 km are smaller in SH25 (Fig. 11d) than those in SH15 (Fig. 8d), leading the θ_e at downshear-right midlevels to decrease more rapidly in SH25 than in SH15 (Figs. 7e and 7f).

The existence of significant potential instability below midlevels in the downshear-right outer core of TCs simulated in SH15 and SH25 implies that continuous forcing is required to convert the potential instability into actual instability in that quadrant. It is hence anticipated that deep convection is generated in the downshear-

Accepted for publication in *Monthly Weather Review*. DOI 10.1175/MWR-D-19-0004.1.

right outer core of a highly sheared TC in the presence of layer lifting by a density current, frontal surface, mesoscale mountain range, and frictional convergence associated with the Ekman pumping due to the outer vortex tilt (Riemer et al. 2010). For example, Hill et al. (1966) pointed out that midlevel dry air intrusions increase the convective instability by reducing humidity and thus θ_e aloft, contributing to landfalling hurricane tornado outbreaks. Although several studies (e.g., McCaul 1987; Curtis 2004) hypothesized midlevel dry intrusions possibly increase the conditional instability by enhancing evaporative cooling and thereby steepening the lapse rate, the lack of latent cooling around midlevels in the downshear-right outer core in SH15 (Fig. 6b) where a weak, dry intrusion forced by the VWS occurs (Fig. 5d) indicates such an evaporative cooling effect is likely limited. The specific relationship between the azimuthally asymmetric potential instability and convective occurrences in the outer core is not addressed here because it is beyond the scope of this study, but it is worth further investigation based on observations and numerical simulations.

c. The θ_e vertical gradient in the downshear-left outer core

The θ_e budget averaged in the downshear-left outer core of the TC simulated in SH15 is first examined. A positive θ_e vertical gradient is seen throughout the whole troposphere in the downshear-left outer core of the TC simulated in SH15 (Figs. 7b, 7e, and 7h), and a potentially stable environment thus exists in that quadrant. Negative θ_e tendencies are predominant in the boundary layer at some times (e.g., 0–20 h and 28–38 h; Fig. 8h), resulting in decreases in θ_e and making the θ_e value within the

Accepted for publication in *Monthly Weather Review*. DOI 10.1175/MWR-D-19-0004.1.

boundary layer relatively lower in the downshear-left quadrant than in other quadrants (Fig. 7b). The θ_e tendency maxima near the midtroposphere (Fig. 8h) become visible after approximately 3 h, and are primarily due to the presence of a shallow layer of enhanced positive horizontal advection at midlevels (Fig. 8e), along with positive vertical advection (Fig. 8f). As a result, there is an increase in θ_e through approximately 30 h and the relatively higher θ_e value in the downshear-left midtroposphere in SH15, compared to other quadrants (Fig. 7e).

The strengthened positive midlevel horizontal advection in the downshear-left quadrant aforementioned (Fig. 8e) is due to horizontal advective contributions of both θ and q_v in the same quadrant (Figs. 9e and 9f). As shown in Figs. 5c and 5d, asymmetric outflow, although relatively weak, prevails in the downshear-left quadrant at midlevels in SH15. As θ and q_v associated with the healthy convection are higher in the inner-core region than in the outer core, the asymmetric outflow transports higher θ and q_v radially outward, leading to downshear-left enhancements of horizontal advection of θ and q_v. Note that the q_v value, which is larger in the downshear-left quadrant than in other quadrants (Fig. 5d), is due to not only the horizontal advection mentioned above but also the vertical moisture transport in the downshear-left quadrant (Fig. 9h). Figure 9 also indicates that, although the vertical advective contributions of θ and q_v counteract each other, net positive vertical advective contributions of the two quantities exist downshear left between z = 1 km and z = 5.5 km (Fig. 8f). As a result, positive θ_e tendency maxima arise in the downshear-left midtroposphere in

Accepted for publication in *Monthly Weather Review*. DOI 10.1175/MWR-D-19-0004.1.

SH15 (Fig. 8h).

As noted in Section 3c, the potential temperatures in the midtropospheric outer core are cooler in the downshear-left quadrant than in other quadrants in SH15 (Fig. 5c). Although latent heating related to the downshear-left updrafts is visible downshear left above the boundary layer (Fig. 6e) and positive horizontal advection exhibits in the downshear-left midtroposphere (Fig. 9e), the vertical advection simultaneously brings about enhanced adiabatic cooling above z = 3 km (Fig. 9g). This negative vertical advection of θ surpasses the latent heating and positive horizontal advection, resulting in lower θ in the downshear-left midtroposphere. Similar findings were also described in Zhang et al. (2002). Nevertheless, the presence of higher mid-tropospheric θ_e values in the downshear-left outer core (Fig. 7e) demonstrates that the positive horizontal advection of both θ and q_v (Figs. 9e and 9f), along with the positive vertical advection of q_v (Fig. 9h) near the midlevels, surpasses the influence of midlevel cold air in that quadrant.

Although positive horizontal advection contributing to the θ_e tendency in the downshear-left quadrant also exists above z = 9 km in SH15 (Fig. 8e), such an advective contribution is weaker than that in the midtroposphere. At upper levels, the warm and moist core of the TC in SH15 is advected more downshear left (Figs. 10c and 10d) than in SH05 (Figs. 10a and 10b), illustrating the strong upper-level advective ventilation effect by the strong asymmetric flow in SH15, as also pointed out in Fu et al. (2019). Although the asymmetric outflow in the downshear-left upper layers (Figs. 10c and 10d)

Accepted for publication in *Monthly Weather Review*. DOI 10.1175/MWR-D-19-0004.1.

is stronger than that near the midtroposphere (Figs. 5c and 5d), positive horizontal advection of θ and q_v in the downshear-left quadrant above z = 9 km is smaller than that around the midlevels (Figs. 9e and 9f) due to the relatively smaller horizontal gradients of θ and q_v in the downshear-left upper layers (Figs. 10c and 10d). The positive horizontal advective contribution to the θ_e tendency in the downshear-left quadrant above z = 9 km is thereby less than that near the midtroposphere in SH15 (Fig. 8e).

The positive contribution by surface fluxes (Fig. 8g) offsets part of the negative effects of advection in the boundary layer (Figs. 8e and 8f), but negative θ_e tendencies sometimes remain evident in the downshear-left boundary layer (Fig. 8h). Downshear-left θ_e is thus reduced and becomes lower in the outer-core boundary layer (Fig. 7b) after the shear is introduced in SH15, compared to the θ_e values in other quadrants. The negative downshear-left horizontal advective contribution to θ_e below z = 3 km (Fig. 8e) results primarily from negative horizontal advection related to q_v (Fig. 9f). In the boundary layer, lower q_v exists left-of-shear because of precipitation-forced downdrafts, and the q_v value decreases radially outward (Fig. 4d). The shear triggers asymmetric inflow in the downshear-left boundary layer (Fig. 4d) and is responsible for negative horizontal advection related to q_v particularly between 100 and 200 km from the TC center in SH15. In contrast, although minimum θ due to evaporative cooling occurs in the downshear-left boundary layer between 100 and 200 km (Fig. 4c), the horizontal advective contribution of θ radially averaged between 100 and 300 km

Accepted for publication in *Monthly Weather Review*. DOI10.1175/MWR-D-19-0004.1.

remains positive in that quadrant (Fig. 9e) because of larger positive θ advection between 200 and 300 km. Additionally, positive vertical advection of θ (Fig. 9g) and more negative vertical advection of q_v confined within the downshear-left boundary layer (Fig. 9h) reflect the presence of low-level downdrafts adjacent to the convective-scale updraft cores in that quadrant (Didlake and Houze 2009; Li and Wang 2012b) and the downward transport of low-entropy air. Consequently, negative net vertical and horizontal advective contributions (Figs. 8e and 8f) partly balance the surface fluxes, resulting jointly in negative θ_e tendencies within the downshear-left boundary layer in SH15 (Fig. 8h).

In the experiment SH25 in which a shear of 25 m s^{-1} is introduced, the θ_e budget results in the downshear-left quadrant mirror those in SH15. The midlevel maximum θ_e tendency is also evident in the downshear-left quadrant in SH25, and it becomes much larger and deeper (Fig. 11h), compared to SH15. The enhancement of the tendency at those levels is because of increases in both horizontal and vertical advection (Figs. 11e and 11f), conducive to the increasing θ_e downshear left (Fig. 7f). Compared to SH15, the asymmetric midlevel outflow of the TC simulated in SH25 is stronger and deeper in the downshear-left quadrant (Figs. 5c, 5f, 7e, and 7f), because of much higher environmental winds from the middle to upper layers in SH25. Large and deep positive horizontal advection of q_v (Fig. 12f) due to the strong asymmetric outflow (Figs. 5f and 7f) in the midtroposphere results in a significantly positive horizontal advective contribution to the θ_e tendency there (Fig. 11e). Although the vertical advection of q_v

Accepted for publication in *Monthly Weather Review*. DOI 10.1175/MWR-D-19-0004.1.

is partly counteracted by vertical advection of θ (Figs. 12g and 12h), the vertical advective contribution to the θ_e tendency in the downshear-left quadrant is still positive between z = 1 km and z = 5.5 km after 6 h (Fig. 11f). As a consequence, positive contributions by both horizontal and vertical advection produce an enhanced positive total θ_e tendency maximum at midlevels in SH25 (Fig. 11h), resulting in the increasing θ_e in the downshear-left midtroposphere (Fig. 7f). Above the altitude of 9 km, significant positive horizontal advection is found as well in the downshear-left quadrant (Fig. 11e), associated with positive horizontal advection of θ and q_v therein (Figs. 12e and 12f) by significant asymmetric outflow (Figs. 7i, 10e, and 10f). On the other hand, the negative θ_e tendencies become more significant in the boundary layer (Fig. 11h) due mainly to the strengthening of negative vertical advection (Fig. 11f), and the value of θ_e diminishes below z = 1 km (Fig. 7c), leading to a larger positive vertical gradient of θ_e and thereby potential stability in the downshear-left quadrant in SH25.

5. Summary

Observations have shown the presence of an azimuthally asymmetric distribution of moist instability in the outer core of sheared TCs. The characteristics and associated physical processes leading to the asymmetric instability are revisited in this study, based on high-resolution idealized numerical simulations of weak (5 m s^{-1}), strong (15 m s^{-1}) and extreme (25 m s^{-1}) shear environments. The simulations demonstrate that a downshear-upshear contrast in CAPE occurs in the outer core of the weakly sheared

Accepted for publication in *Monthly Weather Review*. DOI 10.1175/MWR-D-19-0004.1.

TC, as found in Molinari et al. (2012), with larger (smaller) CAPE in the downshear (upshear) quadrant. Potential instability at low to midlevels is also found in the downshear outer core. A moderate shear (i.e., 10 m s^{-1}) simulation is also conducted, and a similar downshear right–downshear left contrast in moist instability in the outer core is found (not shown). As the shear magnitude increases, a more significant downshear right–downshear left contrast in CAPE is observed, with larger (smaller) values downshear right (left). In addition, potential instability (stability) is present below (above) midlevels in the downshear-right outer core. In the downshear-left outer core, there is a potentially stable environment throughout the troposphere.

As schematically summarized in Fig. 13, downward transports of evaporation-induced, low-entropy air by convective downdrafts in the downshear-left quadrant and by the mesoscale sinking motion underneath the stratiform clouds in the upshear-left quadrant result in lower θ_e within the outer-core boundary layer on the left of the shear vector, particularly in strongly sheared TCs. Because of the much stronger convective downdrafts in the downshear-left quadrant, the lowest boundary-layer θ_e is found there. The absence of sinking motion, along with near-surface fluxes, results in higher θ_e within the downshear-right boundary layer in the outer core. As a result, larger (smaller) CAPE occurs downshear right (left) in the outer core. An interesting feature is the maximum of θ_e at midlevels in the downshear-left quadrant, which is due mainly to the enhanced positive horizontal advection of θ and q_v by the shear-forced asymmetric outflow (Fig. 13). As a result, the positive θ_e vertical gradient produces

Accepted for publication in *Monthly Weather Review*. DOI 10.1175/MWR-D-19-0004.1.

potential stability in the outer core in the downshear-left quadrant. In contrast, the negative vertical gradient of θ_e below the downshear-right midtroposphere in the outer core indicates potential instability there, resulting from the surface fluxes within the boundary layer and the effect of a dry intrusion at the middle to upper levels (Fig. 13).

The above findings indicate that the distribution of boundary-layer θ_e considerably regulates the asymmetry in moist instability in the outer core. Many studies have shown significant asymmetries in boundary-layer θ_e in the inner core of sheared TCs (Riemer et al. 2010; Zhang et al. 2013; Tao and Zhang 2014, 2019). This boundary-layer θ_e asymmetry in the inner core is regularly time-evolving (Riemer et al. 2010; Tao and Zhang 2014, 2019). Low θ_e results from the evaporative cooling of convection associated with the vortex tilt (Riemer et al. 2010; Tao and Zhang 2019), and generally moves downwind due to the advection of the tangential wind (Tao and Zhang 2019). The degree of the boundary-layer θ_e asymmetry in the inner core tends to fade as a result of the vortex alignment due to precession and near-surface entropy recovery due to surface fluxes (Tao and Zhang 2019). In contrast, low θ_e values in the boundary layer in the outer core of strongly sheared TCs persist in the downshear-left quadrant and the θ_e in the outer core is azimuthal-asymmetrically distributed significantly throughout the simulations (Figs. 7b and 7c). Therefore, the azimuthally asymmetric distribution of boundary-layer θ_e in the outer core is relevant to the quasi-stationary principal rainbands in shear (Li et al. 2017), as discussed in the previous

Accepted for publication in *Monthly Weather Review*. DOI 10.1175/MWR-D-19-0004.1.

sections.

The features of azimuthally asymmetric moist instability in the outer core of TCs under environmental vertical shears with different magnitudes are underpinned by numerical simulations in this study, but further observational evidence of the asymmetry sensitive to shear magnitude is needed. It has been uncovered that relatively azimuthally symmetric conditional instability in the outer core can be triggered by outer rainbands of the TC in a stationary environment and evolves with the outer rainband activity (Li and Wang 2012a). The change of such azimuthally symmetric conditional instability, in turn, leads to quasi-periodic behavior of the outer rainbands, which further result in quasi-periodic TC intensity change (Li and Wang 2012a). The relationship between the azimuthally asymmetric moist instability in the outer core of sheared TCs and the initiation and development of convection (e.g., convection in outer rainbands), as well as corresponding TC intensity change, has not been well studied yet, which is thus worth further elaboration. More recently, TC structure and intensity change pertaining to directional environmental shear flows were examined (Nolan 2011; Onderlinde and Nolan 2014, 2016; Gu et al. 2018). How the asymmetric outer-core moist instability behaves in such directional shear flows deserves further investigation as well.

Acknowledgments: The authors thank three anonymous reviewers for helpful comments. This work was jointly supported by the National Key Research and Development Program of China under grant 2017YFC1501601, the

Accepted for publication in *Monthly Weather Review*. DOI 10.1175/MWR-D-19-0004.1.

Key Program of the Ministry of Science and Technology of China under grant 2017YFE0107700, and the National Natural Science Foundation of China under grants 41875054, 41730961, 41730960, and 41775065.

Accepted for publication in *Monthly Weather Review*. DOI 10.1175/MWR-D-19-0004.1.

References:

Barnes, C. E., and G. M. Barnes, 2014: Eye and eyewall traits as determined with the NOAA WP-3D lower-fuselage radar. *Mon. Wea. Rev.*, **142**, 3393–3417.

Barnes, G., E. Zipser, D. Jorgensen, and F. Marks, 1983: Mesoscale and convective structure of a hurricane rainband. *J. Atmos. Sci.*, **40**, 2125–2137.

Black, M. L., J. F. Gamache, F. D. Marks, C. E. Samsury, and H. Willoughby, 2002: Eastern Pacific Hurricanes Jimena of 1991 and Olivia of 1994: The effect of vertical shear on structure and intensity. *Mon. Wea. Rev.*, **130**, 2291–2312.

Corbosiero, K. L., and J. Molinari, 2002: The effects of vertical wind shear on the distribution of convection in tropical cyclones. *Mon. Wea. Rev.*, **130**, 2110–2123.

Corbosiero, K. L., and J. Molinari, 2003: The relationship between storm motion, vertical wind shear, and convective asymmetries in tropical cyclones. *J. Atmos. Sci.*, **60**, 366–376.

Curtis, L., 2004: Mid-level dry intrusions as a factor in tornado outbreaks associated with landfalling tropical cyclones from the Atlantic and Gulf of Mexico. *Wea. Forecasting*, **19**, 411–427.

DeHart, J. C., R. A. Houze, and R. F. Rogers, 2014: Quadrant distribution of tropical

Accepted for publication in *Monthly Weather Review*. DOI 10.1175/MWR-D-19-0004.1.

cyclone inner-core kinematics in relation to environmental shear. *J. Atmos. Sci.,* **71**, 2713–2732.

Didlake, A. C., and R. A. Houze, 2009: Convective-scale downdrafts in the principal rainband of Hurricane Katrina (2005). *Mon. Wea. Rev*., **137**, 3269-3293.

Didlake, A. C., and R. A. Houze, 2013: Dynamics of the stratiform sector of a tropical cyclone rainband. *J. Atmos. Sci.,* **70**, 1891–1911.

Dunion, J. P., 2011: Rewriting the climatology of the tropical North Atlantic and Caribbean Sea atmosphere. *J. Climate,* **24**, 893–908.

Emanuel, K. A., 1994: *Atmospheric Convection*. Oxford University Press, 580 pp.

Fairall, C. W., E. F. Bradley, J. E. Hare, A. A. Grachev, and J. B. Edson, 2003: Bulk parameterization of air–sea fluxes: Updates and verification for the COARE algorithm. *J. Climate*, **16**, 571–591.

Frank, W. M., and E. A. Ritchie, 2001: Effects of vertical wind shear on the intensity and structure of numerically simulated hurricanes. *Mon. Wea. Rev.,* **129**, 2249–2269.

Fu, H., Y. Wang, M. Riemer, and Q. Li, 2019: Effect of unidirectional vertical wind shear on tropical cyclone intensity change—Lower- layer shear versus upper-layer shear. *J. Geophys. Res.*, **124**, https://doi.org/10.1029/2019JD030586.

Accepted for publication in *Monthly Weather Review*. DOI 10.1175/MWR-D-19-0004.1.

Fudeyasu, H., and Y. Wang, 2011: Balanced contribution to the intensification of a tropical cyclone simulated in TCM4: Outer-core spinup process. *J. Atmos. Sci.,* **68**, 430–449.

Gu, J.-F., Z.-M. Tan, and X. Qiu, 2015: Effects of vertical wind shear on inner-core thermodynamics of an idealized simulated tropical cyclone. *J. Atmos. Sci.*, **72**, 511–530.

Gu, J., Z. Tan, and X. Qiu, 2018: The evolution of vortex tilt and vertical motion of tropical cyclones in directional shear flows. *J. Atmos. Sci.,* **75**, 3565–3578.

Hence, D. A., and R. A. Houze, 2008: Kinematic structure of convective-scale elements in the rainbands of Hurricanes Katrina and Rita (2005). *J. Geophys. Res.*, **113**, D15108.

Heng, J., and Y. Wang, 2016: Nonlinear response of a tropical cyclone vortex to prescribed eyewall heating with and without surface friction in TCM4: Implications for tropical cyclone intensification. *J. Atmos. Sci.*, **73**, 1315–1333.

Hill, E. L., W. Malkin, and W. A. Schulz Jr., 1966: Tornadoes associated with cyclones of tropical origin—Practical features. *J. Appl. Meteor.*, **5**, 745–763.

Houze, R. A., 2010: Clouds in tropical cyclones. *Mon. Wea. Rev.*, **138**, 293–344.

Jones, R. W., H. E. Willoughby, and M. T. Montgomery, 2009: Alignment of hurricane-

Accepted for publication in *Monthly Weather Review*. DOI 10.1175/MWR-D-19-0004.1.

like vortices on f and β planes. *J. Atmos. Sci.*, **66**, 1779–1792.

Jones, S. C., 1995: The evolution of vortices in vertical shear. I: Initially barotropic vortices. *Quart. J. Roy. Meteor. Soc.*, **121**, 821–851.

Langland, R. H., and C. S. Liou, 1996: Implementation of an E–ε parameterization of vertical subgrid-scale mixing in a regional model. *Mon. Wea. Rev.,* **124**, 905–918.

Li, Q., and Q. Fang, 2018: A numerical study of convective-scale structures in the outer cores of sheared tropical cyclones. Part 1: Updraft traits in different vertical wind shear magnitudes. *J. Geophys. Res.*, **123**, 12097–12116.

Li, Q., and Y. Wang, 2012a: Formation and quasi-periodic behavior of outer spiral rainbands in a numerically simulated tropical cyclone. *J. Atmos. Sci.,* **69**, 997–1020.

Li, Q., and Y. Wang, 2012b: A comparison of inner and outer spiral rainbands in a numerically simulated tropical cyclone. *Mon. Wea. Rev.*, **140**, 2782–2805.

Li, Q., Y. Wang, and Y. Duan, 2014: Effects of diabatic heating and cooling in the rapid filamentation zone on structure and intensity of a simulated tropical cyclone. *J. Atmos. Sci.,* **71**, 3144–3163.

Li, Q., Y. Wang, and Y. Duan, 2015: Impacts of evaporation of rainwater on tropical cyclone structure and intensity—A revisit. *J. Atmos. Sci.,* **72**, 1323–1345.

Accepted for publication in *Monthly Weather Review*. DOI 10.1175/MWR-D-19-0004.1.

Li, Q., Y. Wang, and Y. Duan, 2017: A numerical study of outer rainband formation in a sheared tropical cyclone. *J. Atmos. Sci.*, **74**, 203–227.

McCaul Jr., E. W., 1987: Observations of Hurricane Danny tornado outbreak of 16 August 1985. *Mon. Wea. Rev.*, **115,** 1206–1223.

Molinari, J., D. M. Romps, D. Vollaro, and L. Nguyen, 2012: CAPE in tropical cyclones. *J. Atmos. Sci.*, **69**, 2452–2463.

Molinari, J., and D. Vollaro, 2008: Extreme helicity and intense convective towers in Hurricane Bonnie. *Mon. Wea. Rev.*, **136,** 4355–4372.

Molinari, J. and D. Vollaro, 2010: Distribution of helicity, CAPE, and shear in tropical cyclones. *J. Atmos. Sci.*, **67**, 274–284.

Moncrieff, M. W., and M. J. Miller, 1976: The dynamics and simulation of tropical cumulonimbus squall lines. *Quart. J. Roy. Meteor. Soc.*, **102,** 373–394.

Nguyen, L. T., R. F. Rogers, and P. D. Reasor, 2017: Thermodynamic and kinematic influences on precipitation symmetry in sheared tropical cyclones: Bertha and Cristobal (2014). *Mon. Wea. Rev.*, **145**, 4423–4446.

Nolan, D. S., 2011: Evaluating environmental favorableness for tropical cyclone development with the method of point-downscaling. *J. Adv. Model. Earth Syst.*, **3**, M08001.

Accepted for publication in *Monthly Weather Review*. DOI 10.1175/MWR-D-19-0004.1.

Onderlinde, M. J., and D. S. Nolan, 2014: Environmental helicity and its effects on development and intensification of tropical cyclones. *J. Atmos. Sci.*, **71**, 4308–4320.

Onderlinde, M. J., and D. S. Nolan, 2016: Tropical cyclone–relative environmental helicity and the pathways to intensification in shear. *J. Atmos. Sci.*, **73**, 869–890.

Powell, M. D., 1990a: Boundary layer structure and dynamics in outer hurricane rainbands. Part I: Mesoscale rainfall and kinematic structure. *Mon. Wea. Rev.*, **118,** 891-917.

Powell, M. D., 1990b: Boundary layer structure and dynamics in outer hurricane rainbands. Part II: Downdraft modification and mixed layer recovery. *Mon. Wea. Rev.*, **118**, 918–938.

Rasmussen, E. N., and D. O. Blanchard, 1998: A baseline climatology of sounding-derived supercell and tornado forecast parameters. *Wea. Forecasting*, **13**, 1148–1164.

Reasor, P. D., M. T. Montgomery, F. D. Marks, and J. F. Gamache, 2000: Low-wavenumber structure and evolution of the hurricane inner-core observed by airborne Dual-Doppler radar. *Mon. Wea. Rev.*, **128**, 1653–1680.

Reasor, P. D., R. Rogers, and S. Lorsolo, 2013: Environmental flow impacts on tropical cyclone structure diagnosed from airborne Doppler radar composites. *Mon.*

Accepted for publication in *Monthly Weather Review*. DOI 10.1175/MWR-D-19-0004.1.

Wea. Rev., **141**, 2949–2969.

Reasor, P. D., M. T. Montgomery, and L. D. Grasso, 2004: A new look at the problem of tropical cyclones in vertical shear flow: Vortex resiliency. *J. Atmos. Sci.*, **61,** 3–22.

Riemer, M. 2016: Meso-β-scale environment for the stationary band complex of vertically sheared tropical cyclones. *Quart. J. Roy. Meteor. Soc.*, **142**, 2442-2451.

Riemer, M., M. T. Montgomery, and M. E. Nicholls, 2010: A new paradigm for intensity modification of tropical cyclones: Thermodynamic impact of vertical wind shear on the inflow layer. *Atmos. Chem. Phys.*, **10**, 3163–3188.

Rios-Berrios, R., and Torn, R. D., 2017: Climatological analysis of tropical cyclone intensity changes under moderate vertical wind shear. *Mon. Wea. Rev.*, **145**, 1717–1738.

Rosenow, A. A., R. M. Rauber, B. F. Jewett, G. M. McFarquhar, and J. M. Keeler, 2018: Elevated potential instability in the comma head: Distribution and development. *Mon. Wea. Rev.,* **146**, 1259–1278.

Rotunno, R., and K. A. Emanuel, 1987: An air–sea interaction theory for tropical cyclones. Part II: Evolutionary study using a nonhydrostatic axisymmetric numerical model. *J. Atmos. Sci.*, **44**, 542–561.

Accepted for publication in *Monthly Weather Review*. DOI 10.1175/MWR-D-19-0004.1.

Schultz, D. M., and P. N. Schumacher, 1999: The use and misuse of conditional symmetric instability. *Mon. Wea. Rev.,* **127**, 2709–2732.

Schultz, D. M., P. N. Schumacher, and C. A. Doswell, 2000: The intricacies of instabilities. *Mon. Wea. Rev.,* **128**, 4143–4148.

Sherwood, S. C., 2000: On moist instability. *Mon. Wea. Rev.,* **128**, 4139–4142.

Stevenson, S. N., K. L. Corbosiero, and J. Molinari, 2014: The convective evolution and rapid intensification of Hurricane Earl (2010). *Mon. Wea. Rev.*, **142,** 4364–4380.

Stevenson, S. N., K. L. Corbosiero, and S. F. Abarca, 2016: Lightning in eastern North Pacific tropical cyclones: A comparison to the North Atlantic. *Mon. Wea. Rev.*, **144**, 225–239.

Tang, B. and K. Emanuel, 2010: Midlevel ventilation's constraint on tropical cyclone intensity. *J. Atmos. Sci.,* **67**, 1817–1830.

Tao, D., and F. Zhang, 2014: Effect of environmental shear, sea surface temperature, and ambient moisture on the formation and predictability of tropical cyclones: An ensemble-mean perspective. *J. Adv. Model. Earth Syst.*, **6**, 384–404.

Tao, D. and F. Zhang, 2019: Evolution of dynamic and thermodynamic structures before and during rapid intensification of tropical cyclones: Sensitivity to vertical

Accepted for publication in *Monthly Weather Review*. DOI 10.1175/MWR-D-19-0004.1.

wind shear. *Mon. Wea. Rev.*, **147**, 1171–1191.

Wadler, J. B., R. F. Rogers, and P. D. Reasor, 2018: The relationship between spatial variations in the structure of convective bursts and tropical cyclone intensification as determined by airborne Doppler radar. *Mon. Wea. Rev.*, **146**, 761–780.

Wang, Y., 2001: An explicit simulation of tropical cyclones with a triply nested movable mesh primitive equation model: TCM3. Part I: Model description and control experiment. *Mon. Wea. Rev.*, **129**, 1370–1394.

Wang, Y., 2002: An explicit simulation of tropical cyclones with a triply nested movable mesh primitive equations model: TCM3. Part II: Model refinements and sensitivity to cloud microphysics parameterization. *Mon. Wea. Rev.*, **130**, 3022–3036.

Wang, Y., 2007: A multiply nested, movable mesh, fully compressible, nonhydrostatic tropical cyclone model – TCM4: Model description and development of asymmetries without explicit asymmetric forcing. *Meteor. Atmos. Phys.*, **97**, 93-116.

Wang, Y., 2008: structure and formation of an annular hurricane simulated in a fully compressible, nonhydrostatic model—TCM4. *J. Atmos. Sci.*, **65**, 1505–1527.

Wang, Y., 2009: How do outer spiral rainbands affect tropical cyclone structure and intensity? *J. Atmos. Sci.*, **66**, 1250–1273.

Accepted for publication in *Monthly Weather Review*. DOI 10.1175/MWR-D-19-0004.1.

Wang, Y., and G. J. Holland, 1996: Tropical cyclone motion and evolution in vertical shear. *J. Atmos. Sci.*, **53**, 3313–3332.

Wang, Y. and J. Xu, 2010: Energy production, frictional dissipation, and maximum intensity of a numerically simulated tropical cyclone. *J. Atmos. Sci.*, **67**, 97–116.

Wang, Y., Y. Rao, Z. Tan, and D. Schönemann, 2015: A statistical analysis of the effects of vertical wind shear on tropical cyclone intensity change over the western North Pacific. *Mon. Wea. Rev.*, **143**, 3434–3453.

Weisman, M. L., and J. B. Klemp, 1982: The dependence of numerically simulated convective storms on vertical wind shear and buoyancy. *Mon. Wea. Rev.*, **110**, 504–520.

Willoughby, H. E., 1988: The dynamics of the tropical cyclone core. *Aust. Meteor. Mag.*, **36**, 183–191.

Willoughby, H. E., F. D. Marks Jr., and R. J. Feinberg, 1984: Stationary and moving convective bands in hurricanes. *J. Atmos. Sci.*, **41**, 505–514.

Xu, Y.-M., and Y. Wang, 2013: On the initial development of asymmetric vertical motion and horizontal relative flow in a mature tropical cyclone embedded in environmental vertical shear. *J. Atmos. Sci.*, **70**, 3471–3491.

Yang, B., Y. Wang, and B. Wang, 2007: The effect of internally generated inner-core

Accepted for publication in *Monthly Weather Review*. DOI 10.1175/MWR-D-19-0004.1.

asymmetries on tropical cyclone potential intensity. *J. Atmos. Sci.*, **64**, 1165–1188.

Zhang, D., Y. Liu, and M. K. Yau, 2002: A multiscale numerical study of Hurricane Andrew (1992). Part V: Inner-core thermodynamics. *Mon. Wea. Rev.*, **130**, 2745–2763.

Zhang, J. A., and R. F. Rogers, 2019: Effects of parameterized boundary layer structure on hurricane rapid intensification in shear. *Mon. Wea. Rev.,* **147**, 853–871.

Zhang, J. A., R. F. Rogers, P. D. Reasor, E. W. Uhlhorn, and F. D. Marks, 2013: Asymmetric hurricane boundary layer structure from dropsonde composites in relation to the environmental vertical wind shear. *Mon. Wea. Rev.*, **141**, 3968–3984.

Accepted for publication in *Monthly Weather Review*. DOI 10.1175/MWR-D-19-0004.1.

Table caption:

Table 1. Brief description of physical parameterizations in TCM4.

Accepted for publication in *Monthly Weather Review*. DOI 10.1175/MWR-D-19-0004.1.

Figure captions:

Figure 1. Time series of the simulated minimum surface pressure (hPa) of TCs in SH05 (black line), SH15 (blue line), and SH25 (red line) after vertical shears are imposed. The inset displays VWS profiles corresponding to shear magnitudes of 5, 15, and 25 m s^{-1}. Note that the minimum surface pressure in SH25 is only shown for the first 12 hours, after which the storm in that experiment decays.

Figure 2. CAPE (shading; J kg^{-1}) and 3-km-height reflectivity (contours; dBZ) of the TCs simulated in (a) SH05 at 24 h, (b) SH15 at 24 h, and (d) SH25 at 9 h. Reflectivity is contoured at 10, 20, 30, and 45 dBZ with lighter colors indicating larger values. Black dashed concentric circles are every 100 km from the TC center, and shear direction is indicated by the black arrow.

Figure 3. Time-azimuth distributions of CAPE (top panels; J kg^{-1}) and CIN (bottom panels; J kg^{-1}) radially averaged between 100 and 300 km for (a), (d) SH05, (b), (e) SH15, and (c), (f) SH25. "UL", "UR", "DR", and "DL" denote shear-relative quadrants of upshear left, upshear right, downshear right, and downshear left, respectively. Note that the results after 12 h in SH25 are excluded in (c), and (f) because the modeled TC decays after that time.

Figure 4. θ (left column; shading; unit: K) and q_v (right column; shading; unit: g kg^{-1}) vertically averaged between z = 0.1 and 0.96 km and temporally averaged between 0 and 48 h in (a–b) SH05, (c–d) SH15, and averaged between 0 and 12 h

Accepted for publication in *Monthly Weather Review*. DOI 10.1175/MWR-D-19-0004.1.

in (e–f) SH25, superposed by asymmetric winds (black vectors). Black dashed concentric circles are every 100 km from the TC center, and shear direction is indicated by the balck arrow.

Figure 5. As in Fig. 4, but for quantities vertically averaged between z = 4.3 and 5.0 km. Note that scales of the color bars are different from those in Fig. 4.

Figure 6. Time-height cross sections of mean (radially averaged between 100 and 300 km) latent heating rate (K h^{-1}) in SH05 (first column), SH15 (second column), and SH25 (third column). Condensational heating for the downshear-right, downshear-left, upshear-left, and upshear-right quadrants are depicted in the (a–c) first, (d–f) second, (g–i) third, and (j–l) fourth rows, respectively. Note that the stippling indicates sinking regions.

Figure 7. Time-azimuth distributions of θ_e (shading; unite: K) radially averaged between 100 and 300 km, superposed by asymmetric radial flows (arrows). Top panels show values vertically averaged between z = 0.1 and 0.96 km along with asymmetric inflows, middle panels show values vertically averaged between z = 4.3 and 5.0 km along with asymmetric outflows, and bottom panels display values vertically averaged between z = 9.6 and 10.6 km along with asymmetric outflows for (a), (d), (g) SH05, (b), (e), (h) SH15, and (c), (f), (i) SH25. Note that the results after 12 h in SH25 are excluded in (c), (f), and (i), because the modeled TC decays after that time.

Accepted for publication in *Monthly Weather Review*. DOI 10.1175/MWR-D-19-0004.1.

Figure 8. Time-height cross sections of mean (radially averaged between 100 and 300 km) contributions to the θ_e tendency (K h^{-1}) in SH15 by the horizontal advection (first column), vertical advection (second column), and diabatic processes (third column). The panels in the fourth column show total θ_e tendency. Budget results for the downshear-right, downshear-left, upshear-left, and upshear-right quadrants are depicted in the (a–d) first, (e–h) second, (i–l) third, and (m–p) fourth rows, respectively.

Figure 9. Time-height cross sections of mean (radially averaged between 100 and 300 km) contributions to the θ_e tendency (K h^{-1}) in SH15 by the horizontal advection of θ (first column), horizontal advection associated with q_v (second column), vertical advection of θ (third column), and vertical advection associated with q_v (fourth column). Results for the downshear-right, downshear-left, upshear-left, and upshear-right quadrants are depicted in the (a–d) first, (e–h) second, (i–l) third, and (m–p) fourth rows, respectively.

Figure 10. As in Fig. 4, but for quantities vertically averaged between z = 9.6 and 10.6 km. Note that scales of the color bars are different from those in Fig. 4.

Figure 11. As in Fig. 8, but for SH25.

Figure 12. As in Fig. 9, but for SH25.

Figure 13. Three-dimensional schematic summarizing the processes causing

Accepted for publication in *Monthly Weather Review*. DOI 10.1175/MWR-D-19-0004.1.

azimuthally asymmetric moist instability in the outer core of a sheared TC.

Accepted for publication in *Monthly Weather Review*. DOI 10.1175/MWR-D-19-0004.1.

TABLE 1. Brief description of physical parameterizations in TCM4.

Basic model physics	Description
Cumulus parameterization	No
Cloud microphysics	Explicit mixed-phase cloud microphysics (Wang 2001)
Surface layer scheme	Modified Monin–Obukhov scheme (Fairall et al. 2003; Wang 2002)
Subgrid-scale vertical turbulent mixing	*E*–ε turbulence closure scheme (Langland and Liou 1996)
Longwave radiative cooling	A Newtonian cooling term added to the perturbation potential temperature equation (Rotunno and Emanuel 1987)

Accepted for publication in *Monthly Weather Review*. DOI 10.1175/MWR-D-19-0004.1.

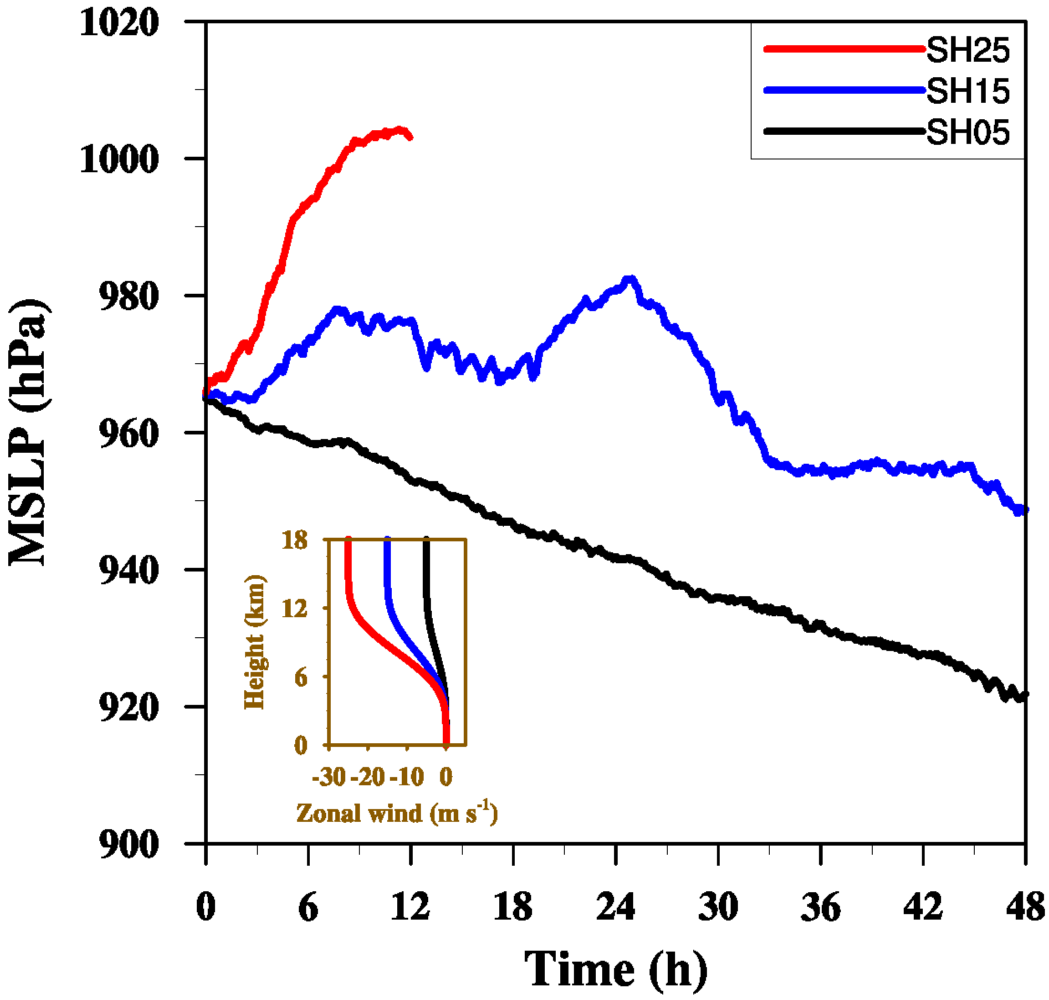

FIG. 1. Time series of the simulated minimum surface pressure (hPa) of TCs in SH05 (black line), SH15 (blue line), and SH25 (red line) after vertical shears are imposed. The inset displays VWS profiles corresponding to shear magnitudes of 5, 15, and 25 m s^{-1}. Note that the minimum surface pressure in SH25 is only shown for the first 12 hours after, which the storm in that experiment decays.

Accepted for publication in *Monthly Weather Review*. DOI 10.1175/MWR-D-19-0004.1.

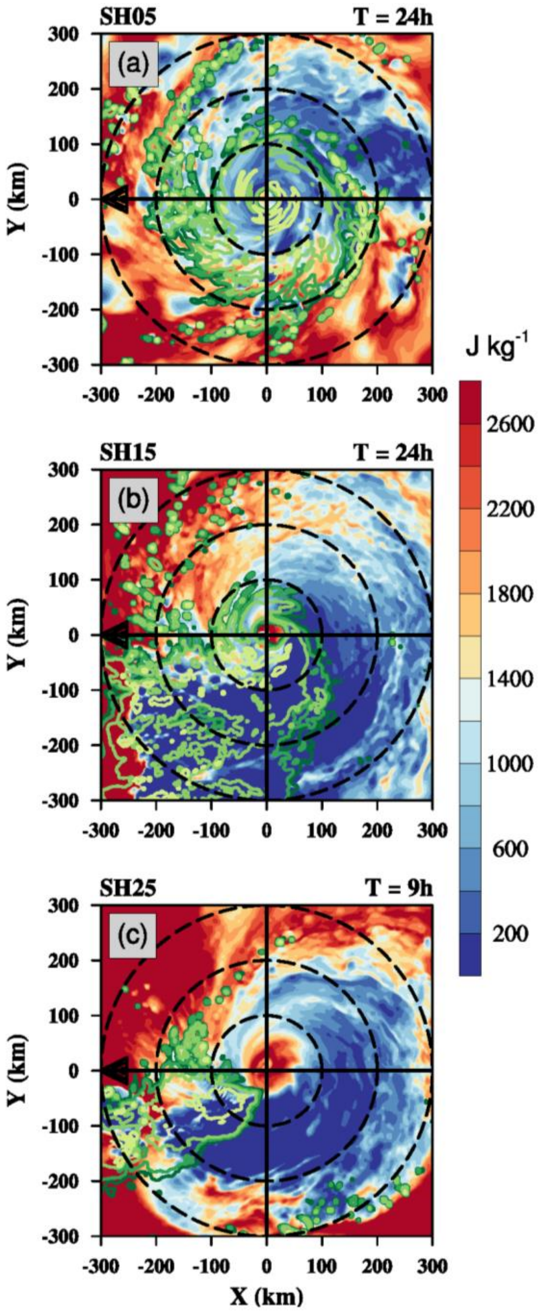

FIG. 2. CAPE (shading; J kg^{-1}) and 3-km-height reflectivity (contours; dBZ) of the TCs simulated in (a) SH05 at 24 h, (b) SH15 at 24 h, and (d) SH25 at 9 h. Reflectivity is contoured at 10, 20, 30, and 45 dBZ with lighter colors indicating larger values. Black dashed concentric circles are every 100 km from the TC center, and shear direction is indicated by the black arrow.

Accepted for publication in *Monthly Weather Review*. DOI 10.1175/MWR-D-19-0004.1.

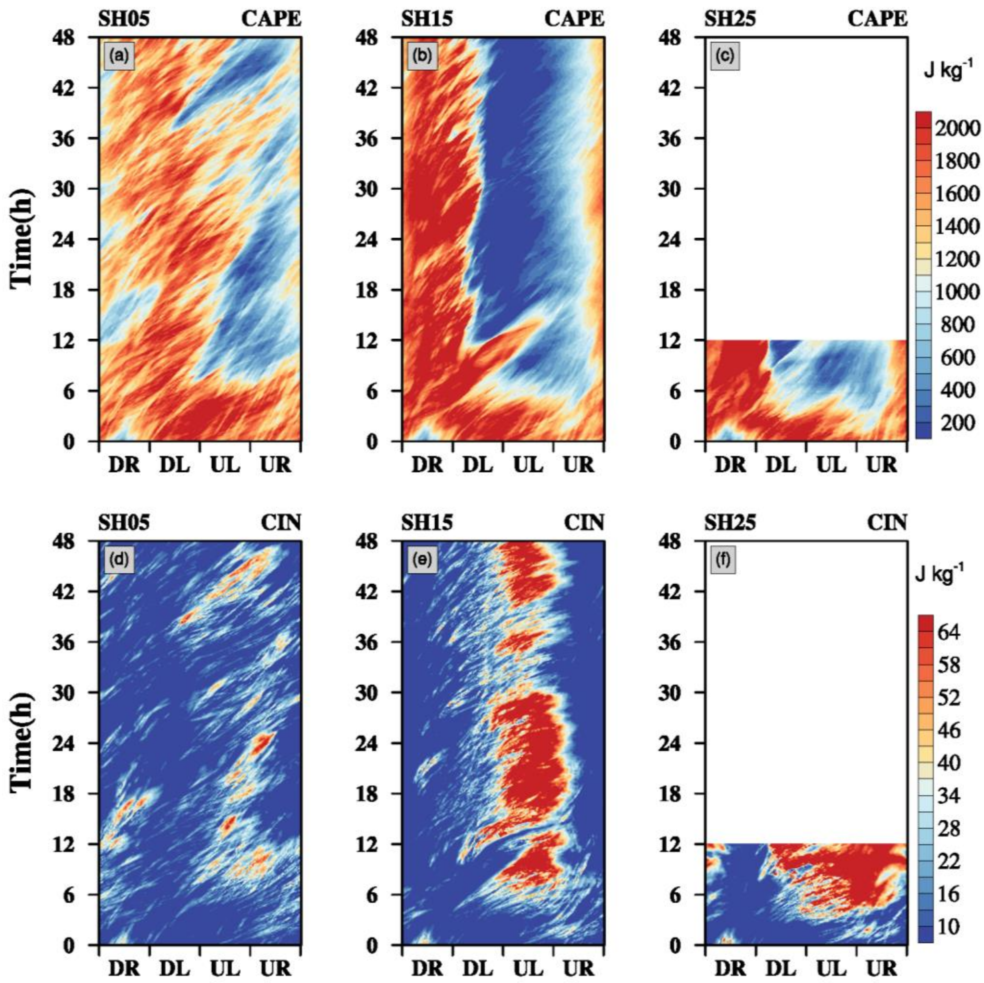

FIG. 3. Time-azimuth distributions of CAPE (top panels; J kg^{-1}) and CIN (bottom panels; J kg^{-1}) radially averaged between 100 and 300 km for (a), (d) SH05, (b), (e) SH15, and (c), (f) SH25. "UL", "UR", "DR", and "DL" denote shear-relative quadrants of upshear left, upshear right, downshear right, and downshear left, respectively. Note that the results after 12 h in SH25 are excluded in (c), and (f) because the modeled TC decays after that time.

Accepted for publication in *Monthly Weather Review*. DOI 10.1175/MWR-D-19-0004.1.

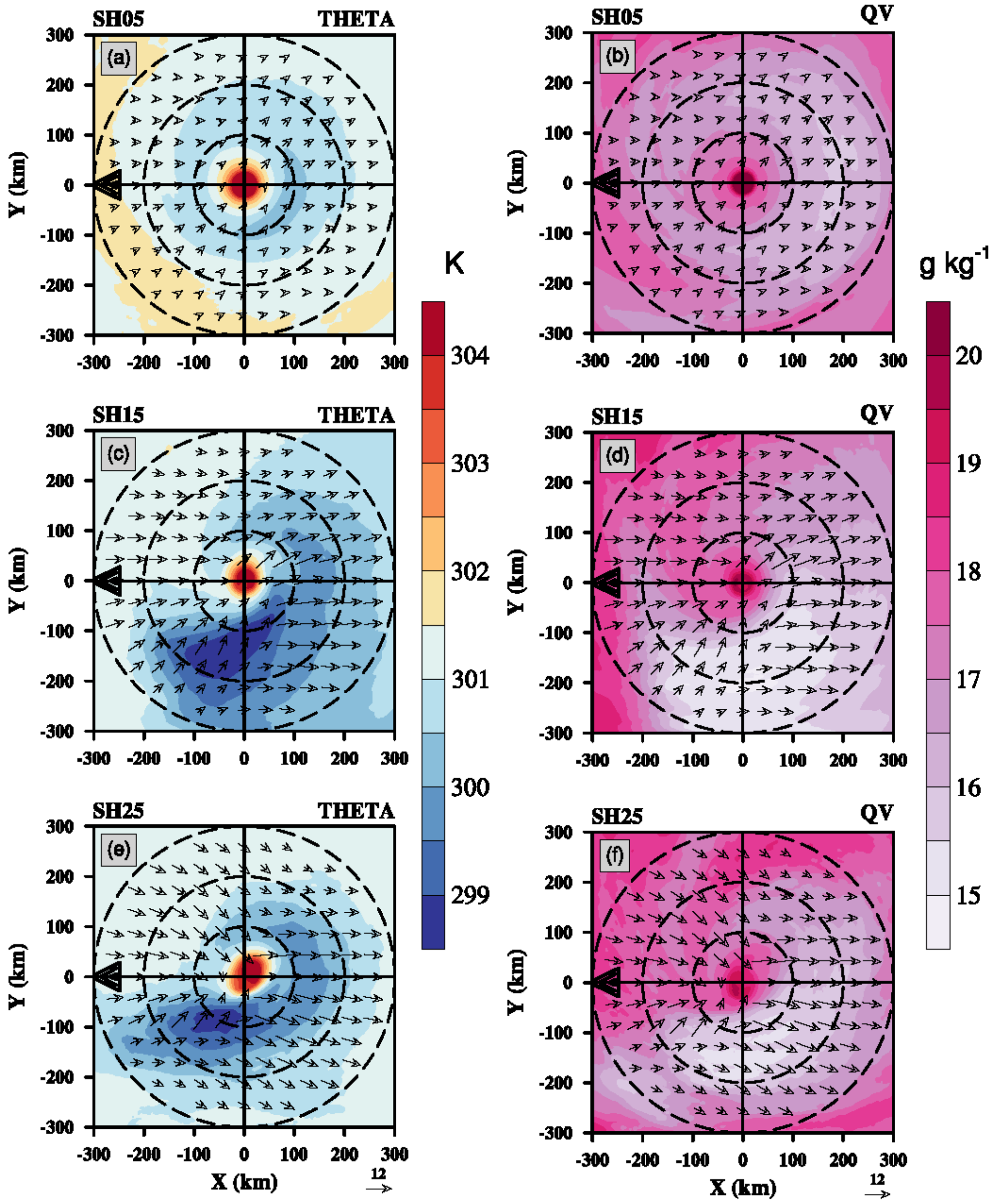

FIG. 4. θ (left column; shading; unit: K) and q_v (right column; shading; unit: g kg^{-1}) vertically averaged between z = 0.1 and 0.96 km and temporally averaged between 0 and 48 h in (a–b) SH05, (c–d) SH15, and averaged between 0 and 12 h in (e–f) SH25, superposed by asymmetric winds (black vectors). Black dashed concentric circles are every 100 km from the TC center, and shear direction is indicated by the black arrow.

Accepted for publication in *Monthly Weather Review*. DOI 10.1175/MWR-D-19-0004.1.

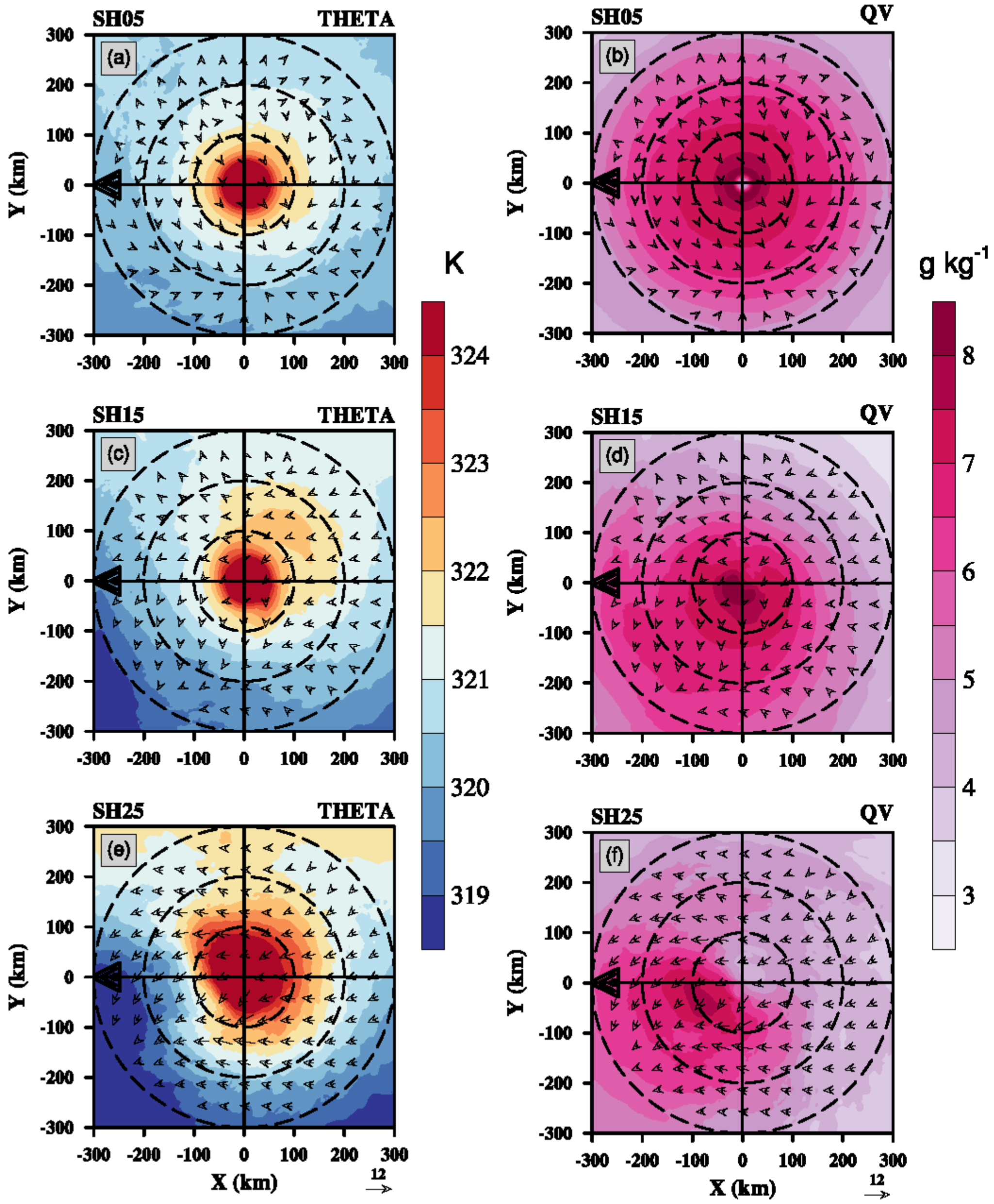

FIG. 5. As in Fig. 4, but for quantities vertically averaged between z = 4.3 and 5.0 km. Note that scales of the color bars are different from those in Fig. 4.

Accepted for publication in *Monthly Weather Review*. DOI 10.1175/MWR-D-19-0004.1.

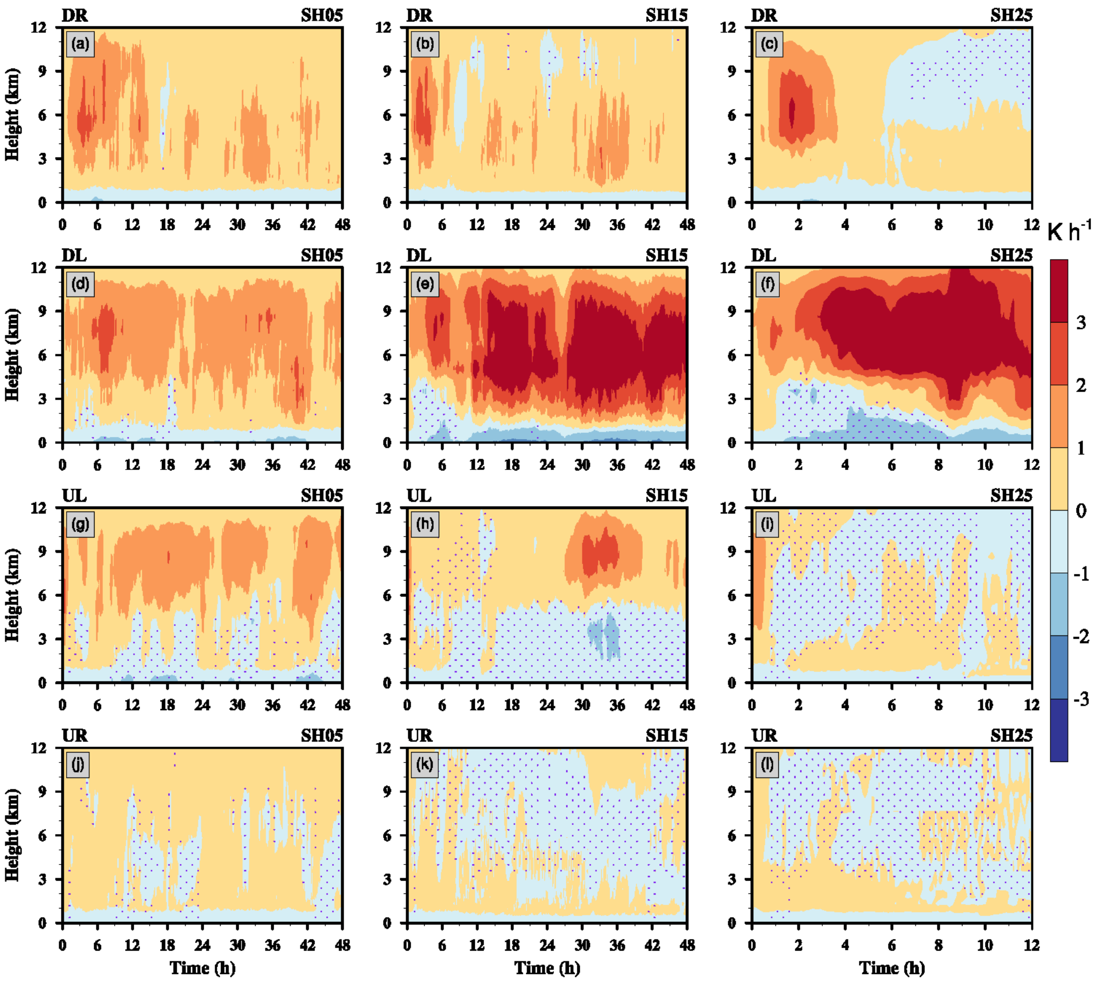

FIG. 6. Time-height cross sections of mean (radially averaged between 100 and 300 km) latent heating rate (K h^{-1}) in SH05 (first column), SH15 (second column), and SH25 (third column). Condensational heating for the downshear-right, downshear-left, upshear-left, and upshear-right quadrants are depicted in the (a–c) first, (d–f) second, (g–i) third, and (j–l) fourth rows, respectively. Note that the stippling indicates sinking regions.

Accepted for publication in *Monthly Weather Review*. DOI 10.1175/MWR-D-19-0004.1.

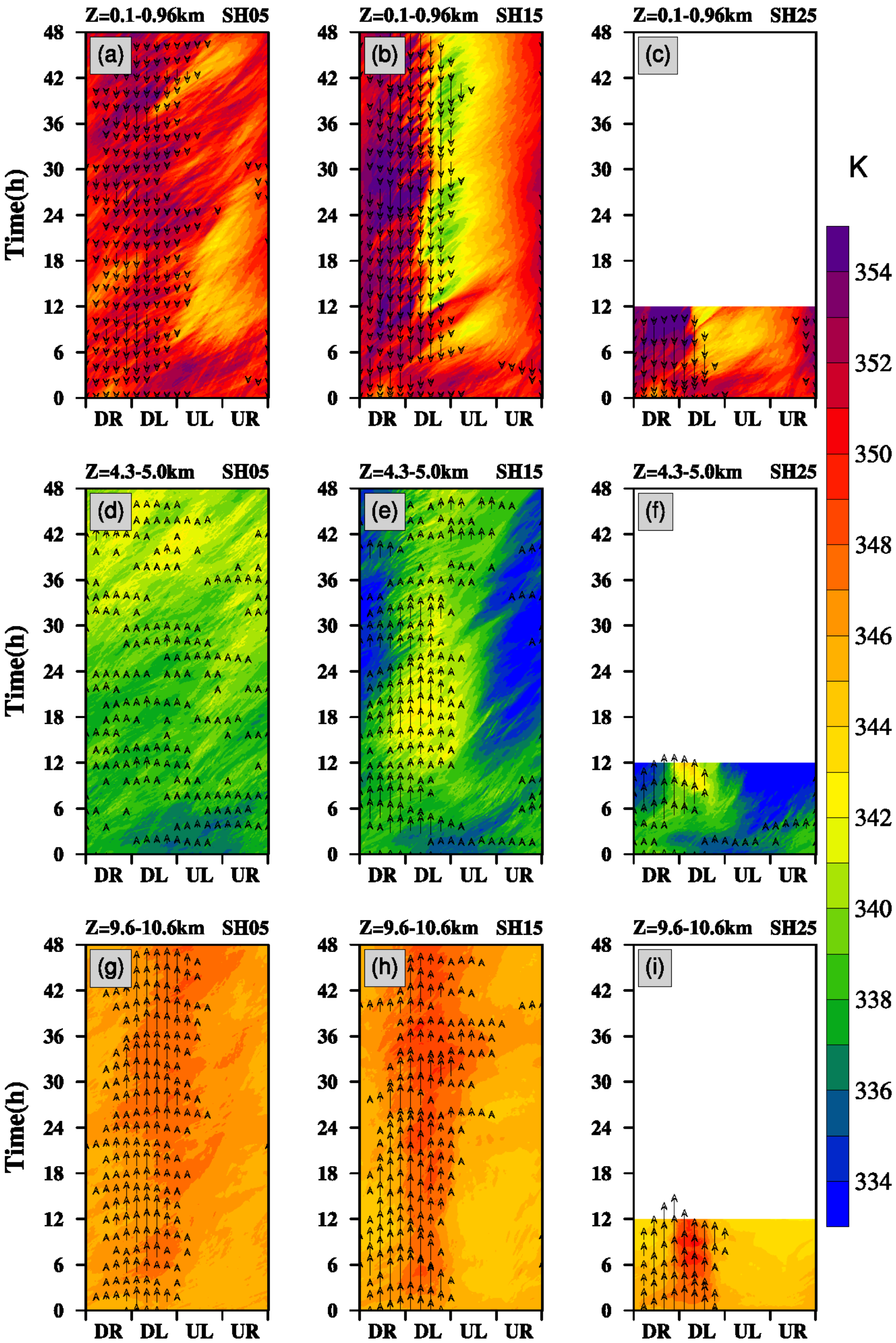

978 ↓ **inflow:** 10m/s ↑ **outflow:** 10m/s

979 FIG. 7. Time-azimuth distributions of θ_e (shading; unite: K) radially averaged

Accepted for publication in *Monthly Weather Review*. DOI 10.1175/MWR-D-19-0004.1.

between 100 and 300 km, superposed by asymmetric radial flows (arrows). Top panels show values vertically averaged between z = 0.1 and 0.96 km along with asymmetric inflows, middle panels show values vertically averaged between z = 4.3 and 5.0 km along with asymmetric outflows, and bottom panels display values vertically averaged between z = 9.6 and 10.6 km along with asymmetric outflows for (a), (d), (g) SH05, (b), (e), (h) SH15, and (c), (f), (i) SH25. Note that the results after 12 h in SH25 are excluded in (c), (f), and (i), because the modeled TC decays after that time.

Accepted for publication in *Monthly Weather Review*. DOI 10.1175/MWR-D-19-0004.1.

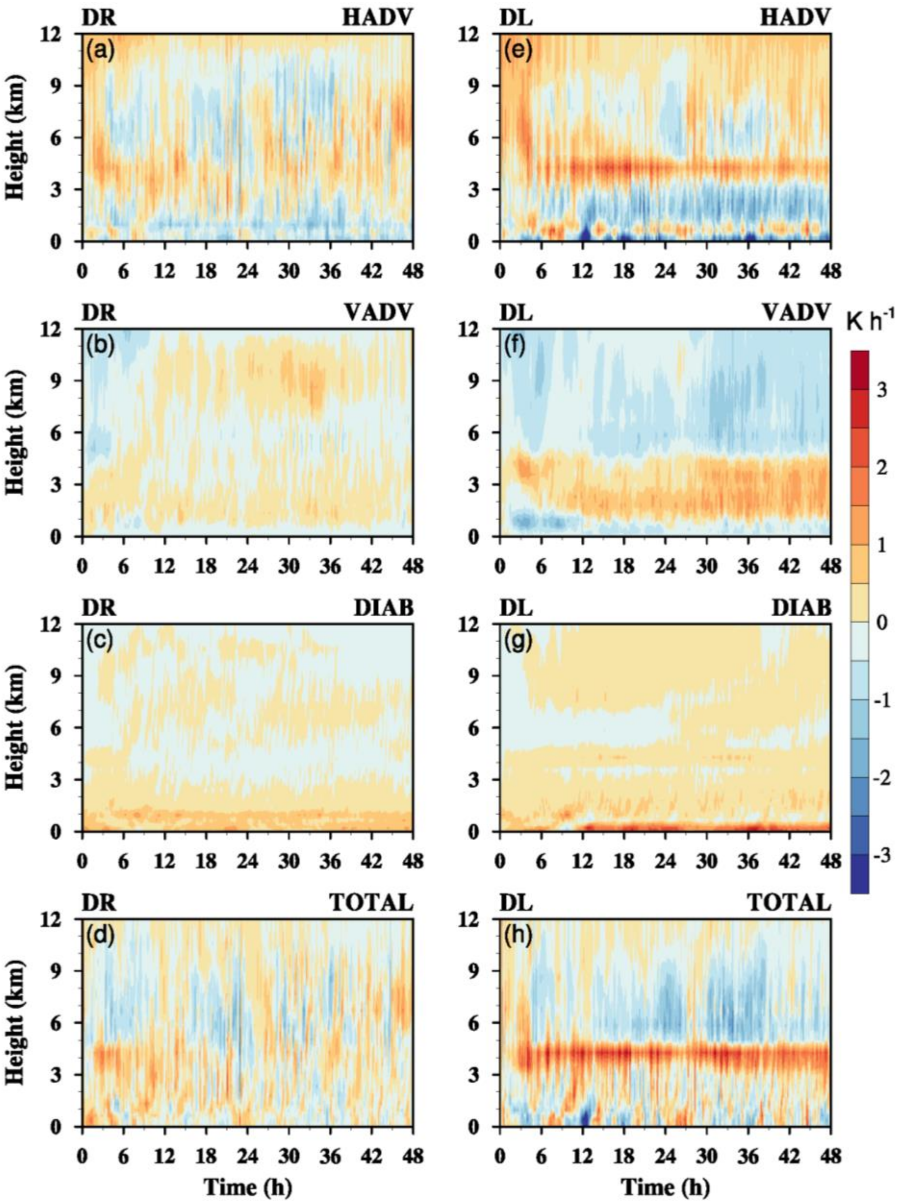

FIG. 8. Time-height cross sections of mean (radially averaged between 100 and 300 km) contributions to the θ_e tendency (K h^{-1}) in SH15 by the horizontal advection (first row), vertical advection (second row), and diabatic processes (third row). The panels in the fourth row show total θ_e tendency. Budget results for the downshear-right and downshear-left quadrants are depicted in the (a–d) left and (e–h) right columns, respectively.

Accepted for publication in *Monthly Weather Review*. DOI 10.1175/MWR-D-19-0004.1.

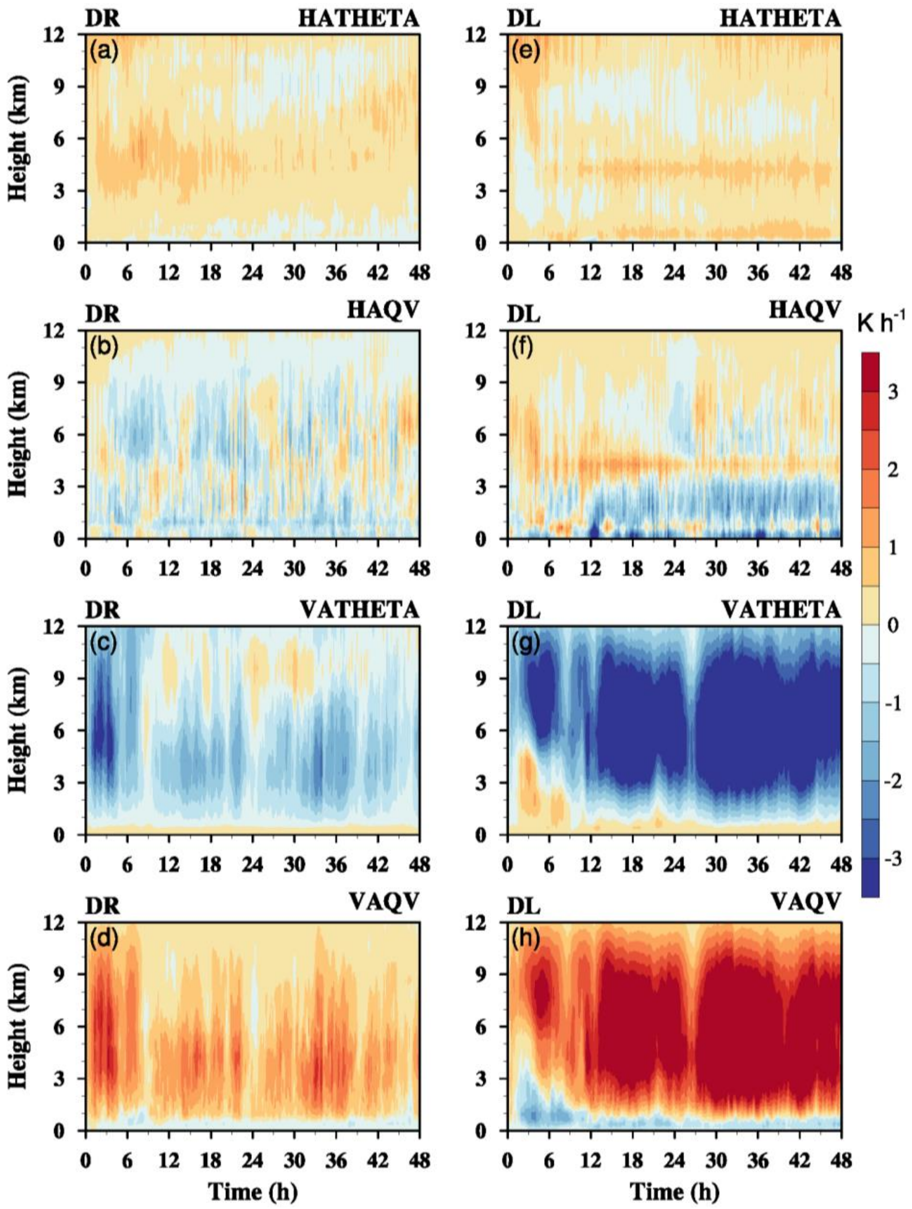

FIG. 9. Time-height cross sections of mean (radially averaged between 100 and 300 km) contributions to the θ_e tendency (K h^{-1}) in SH15 by the horizontal advection of θ (first row), horizontal advection associated with q_v (second row), vertical advection of θ (row), and vertical advection associated with q_v (fourth row). Results for the downshear-right and downshear-left quadrants are depicted in the (a–d) left and (e–h) right columns, respectively.

Accepted for publication in *Monthly Weather Review*. DOI 10.1175/MWR-D-19-0004.1.

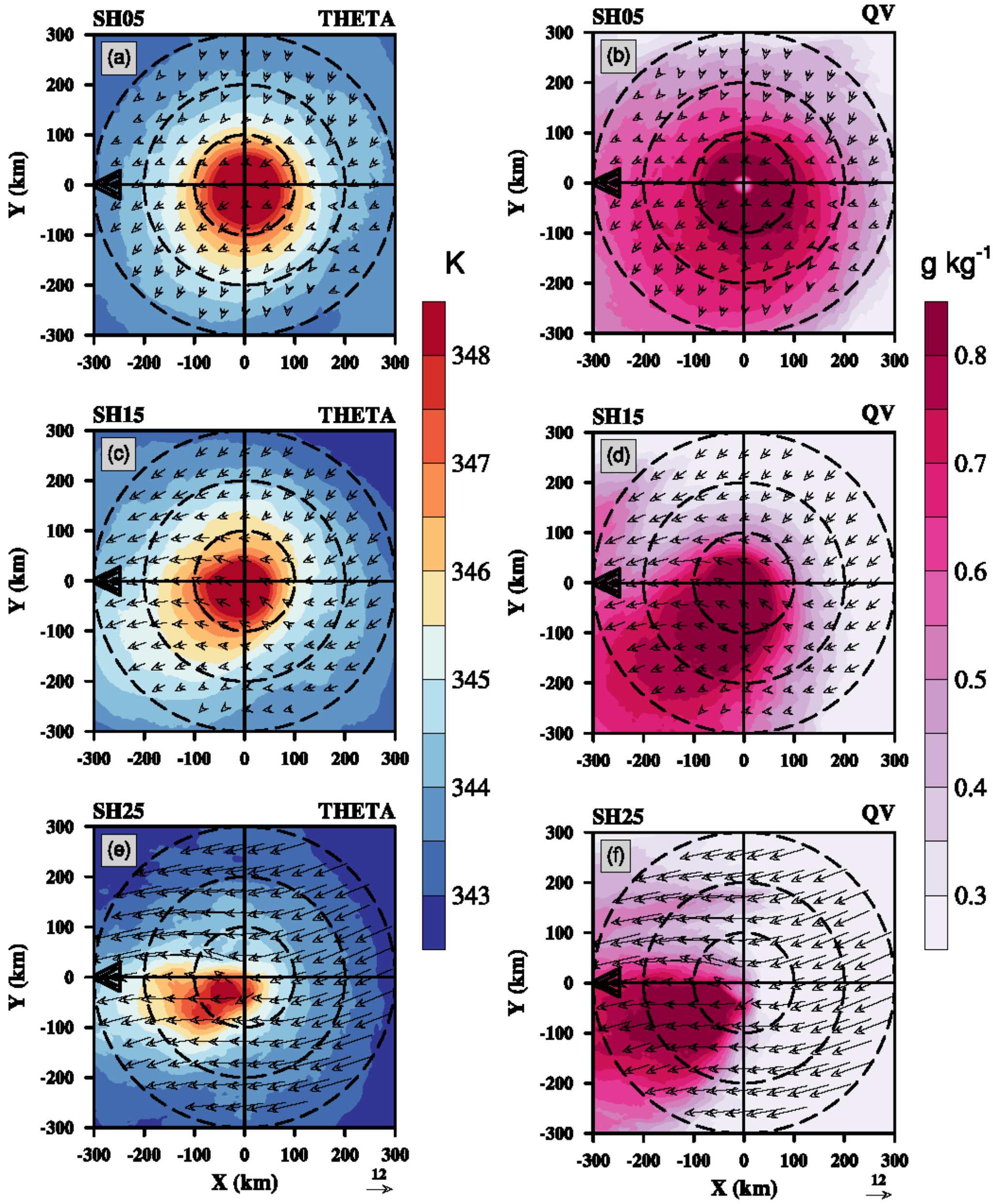

FIG. 10. As in Fig. 4, but for quantities vertically averaged between z = 9.6 and 10.6 km. Note that scales of the color bars are different from those in Fig. 4.

Accepted for publication in *Monthly Weather Review*. DOI 10.1175/MWR-D-19-0004.1.

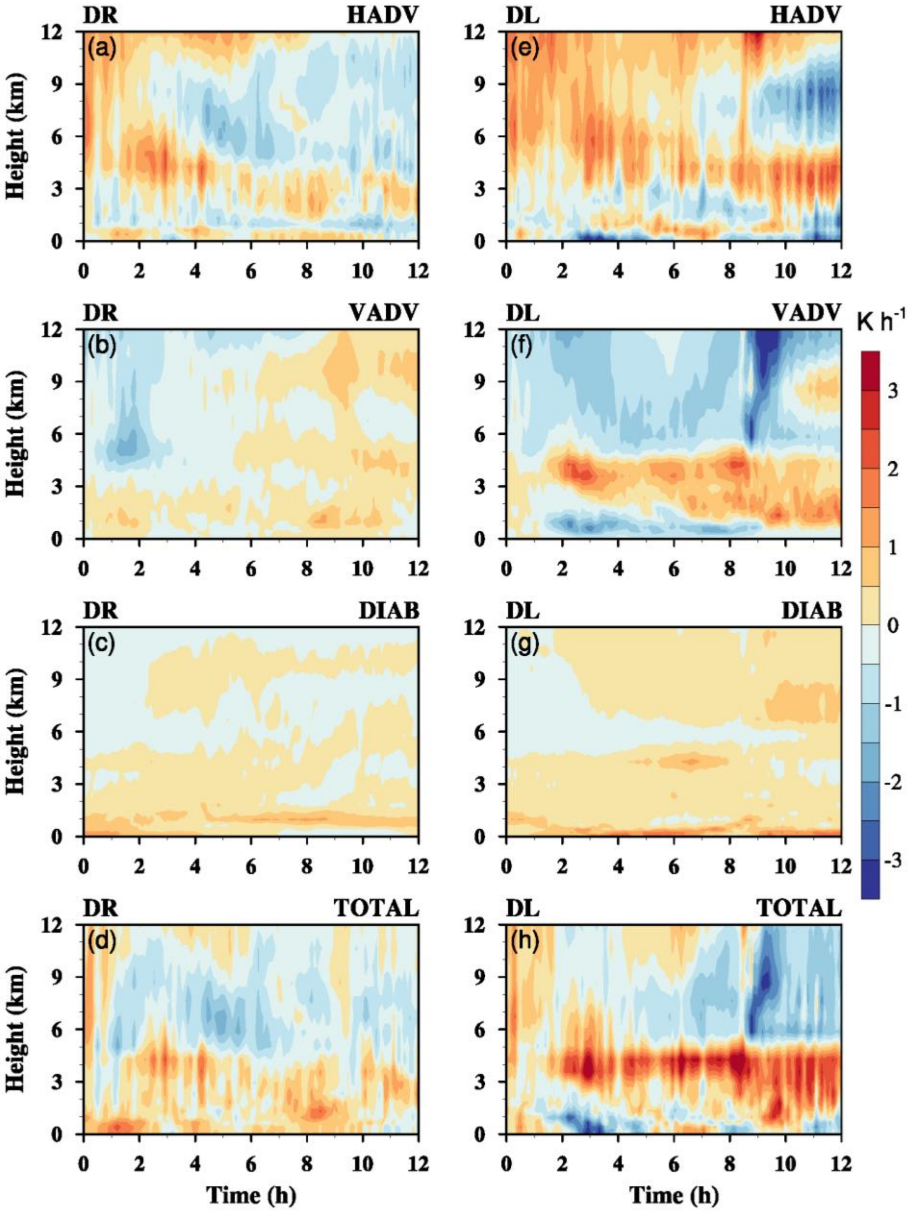

FIG. 11. As in Fig. 8, but for SH25.

Accepted for publication in *Monthly Weather Review*. DOI 10.1175/MWR-D-19-0004.1.

1007 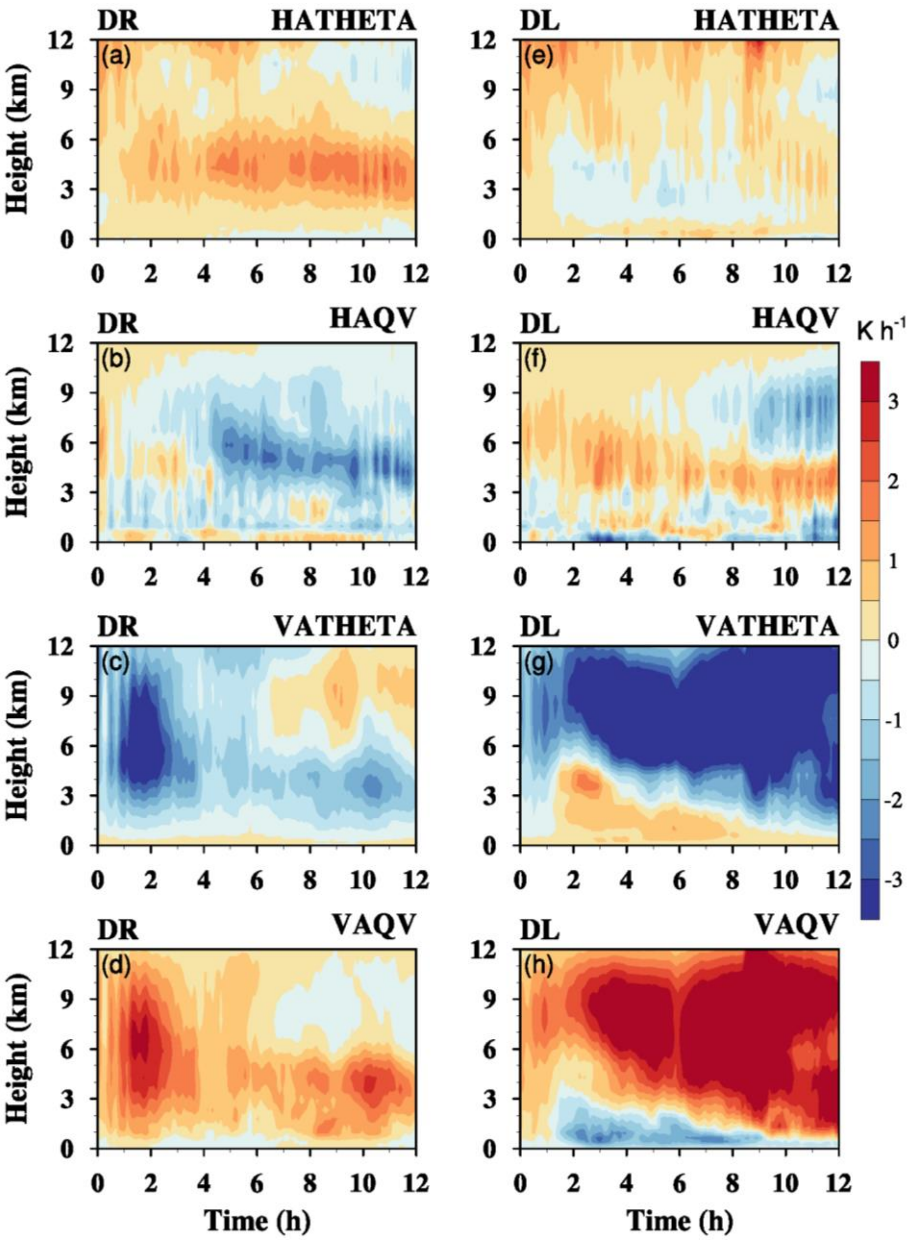

1008 FIG. 12. As in Fig. 9, but for SH25.

Accepted for publication in *Monthly Weather Review*. DOI 10.1175/MWR-D-19-0004.1.

1009

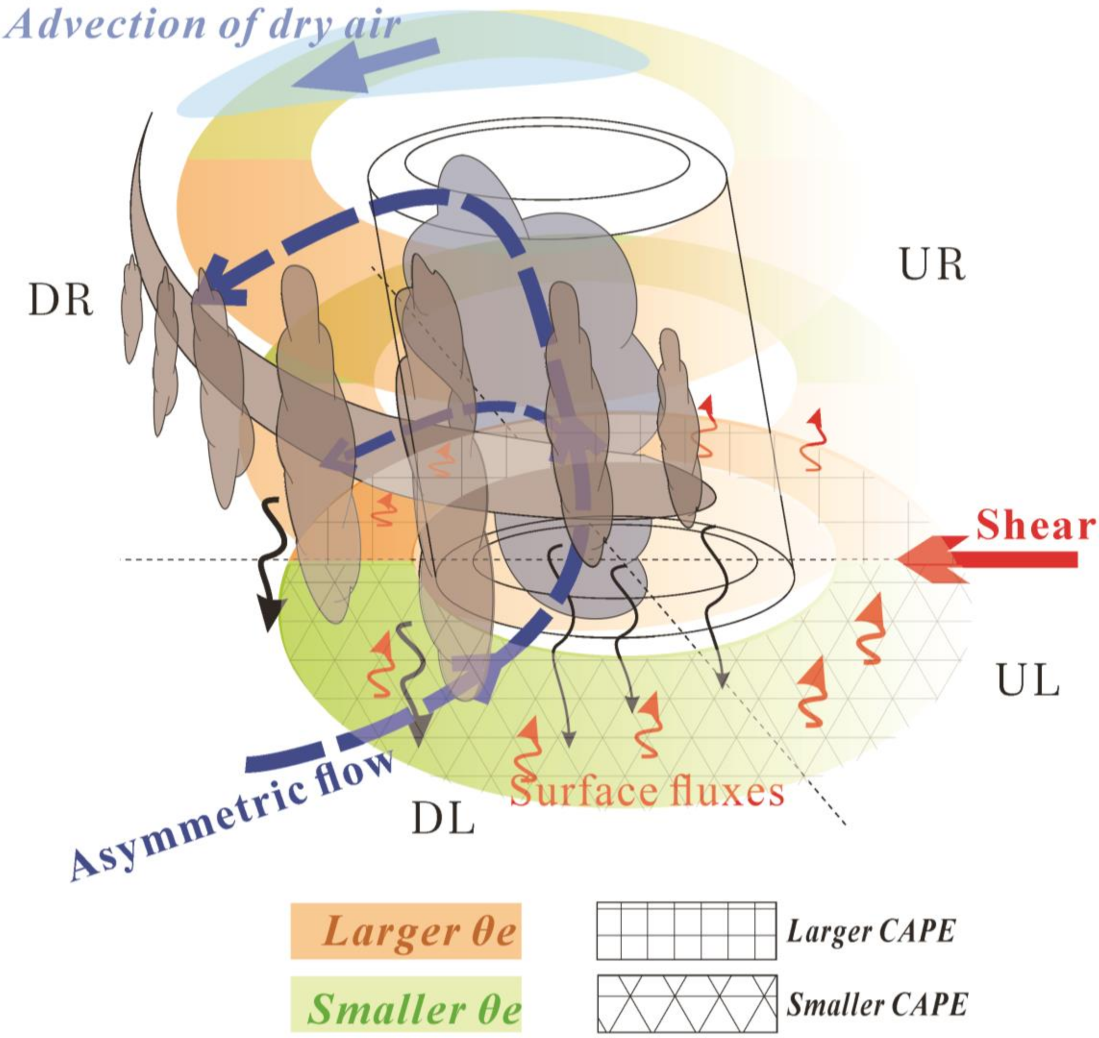

1010 FIG. 13. Three-dimensional schematic summarizing the processes causing

1011 azimuthally asymmetric moist instability in the outer core of a sheared TC.

Accepted for publication in *Monthly Weather Review*. DOI 10.1175/MWR-D-19-0004.1.